NORMAL FAULT GROWTH IN THREE DIMENSIONS

A THESIS SUBMITTED TO THE GRADUATE DIVISION OF THE UNIVERSITY OF HAWAI'I IN PARTIAL FULFILLMENT OF THE REQUIREMENTS FOR THE DEGREE OF

Master of Science

in

Geology and Geophysics

May 2004

By

Joern Ole Kaven

Thesis Committee:

Steven J. Martel, Chairperson

Jane M. Becker

Garrett Ito

Acknowledgements

I would like to thank Steve Martel who has been a great advisor. His guidance, patience and support is unparalleled. I would also like to thank Janet Becker and Garrett Ito for their contributions to this thesis. The support of this research by the U.S. Department of Energy (Grant number DE-FG03-95ER14525) is greatly appreciated.

I would like to thank my family, in particular my Mom, who endured many years of separation and to this day remains very supportive. I am also very grateful for the love and support of Jessica Sudduth.

Contents

I Evolution of Surface-Breaching Normal Faults 1

Abstract 2

1 Introduction 3

2 Field Observations 7

2.1 Koae Fault System 7

2.2 Hopena Fault 7

3 Mechanical Analysis of Near-Fault Deformation 14

3.1 Model Fault Geometry 14

3.2 Ambient Stress Field and Boundary Conditions 16

3.3 Boundary Element Method 20

3.4 Results 21

3.4.1 Downward Growth 22

3.4.2 Upward Growth 25

4 Discussion 35

5 Conclusions 40

II Evolution of Normal Fault Tiplines 41

Abstract 42

1 Introduction 43

2 Field Data and Kinematics 45

3 Mechanical Analysis of Tipline Evolution **47**

3.1 Model Fault Geometry 47

3.2 Propagation Tendencies 48

3.3 Ambient Stress Field and Fault 51

3.4 Boundary Element Method 54

3.5 Results 56

4 Conclusions **60**

A Appendix **61**

A.1 Analytical Solution for $\mathcal{G}$ in a Full-Space 61

A.2 Stress Orientations for Varied Boundary Conditions 63

List of Figures

1 Aerial photo map of the central and western Koae fault system 5

2 Structural map of the northern fork of the Hopena Fault 5

3 Hopena fault scarp 9

4 Profiles across the scarp of the north fork of the Hopena fault 11

5 Fracture strikes and trends of horizontal relative displacements 12

6 Relative displacements on fractures 13

7 Fracture modes 15

8 Model fault geometries 16

9 Boundary element patterns on model faults 17

10 Reference frames 19

11 Representation of boundary value problem 20

12 Oblique view of vertical surface displacements for faults nucleating at the surface 23

13 Oblique view of vertical surface displacements for faults nucleating at the surface 24

14 Oblique view of vertical surface displacements for an isolated fault . . 26

15 Surface stress fields near an isolated fault growing up from depth . . 27

16 Surface stress fields near the end of faults at various depth 29

17 Oblique view of vertical surface displacements for a fault with nearby fissure 30

18 Surface stress fields near fault growing up from depth and a fissure . . 31

19 Most tensile stress in vertical slices 33

20 Along strike view of fault, fissure, and antithetic structure 34

21 Stress field near a fault, a fissure, and an antithetic fracture 34

22 Stress rotation near trace ends 36

23 Growth history 38

24 Single model fault 48

25 Along strike view of fault, fissure, and antithetic structure 48
26 Fracture modes 50
27 Reference frames 53
28 Representation of boundary value problem 55
29 Propagation tendencies for isolated fault 57
30 Propagation tendencies for fault and fissure 58
31 Propagation tendencies for fault and antithetic fractures 59
32 Locations of γ, ω, σ, θ, a and b 62
33 Stress trajectories of varied boundary conditions 64

Part I

Evolution of Surface-Breaching Normal Faults

Abstract

Surface deformation along scarps of active normal faults on Kilauea volcano, Hawaii, provides evidence for how the faults grow. Deformation near the east end of an east-striking fault that dips to the north has been mapped in detail. The scarp is a breached monocline, with a gentle monoclinal flexure extending past the end of the fault scarp trace. Fractures on the monocline form an echelon pattern. Monocline fractures strike east-northeast near the end of the fault and along the monocline. Belts of fractures characteristically form on both the uplifted footwall and the hangingwall, with a belt of buckles forming between the fault scarp and the hangingwall fractures. Fissures on the footwall have apertures about three times larger than those on the hangingwall. The belts of fractures and buckles are roughly parallel to the fault scarp away from the fault scarp ends, but these belts converge towards the end of the scarp trace. Away from the scarp end, fissures on the footwall generally strike roughly sub-parallel to the fault. Near the scarp trace end, the fissures form a pronounced echelon pattern. They strike east-northeast near the end of the fault.

Three-dimensional boundary element analyses show that slip on blind elliptical faults generates a monoclinal flexure of the ground surface. Fissures on the footwall and fractures along the scarp are consistent with a predicted tensile stress concentration above an isolated fault. Hangingwall fractures can be accounted for by the inclusion of an antithetic fracture at the upper tipline of a blind fault. High compressive stresses at the base of the scarp indicate a fault-parallel trend of buckles, consistent with the field observations. Modeling also indicates that fractures along the scarp that open in response to slip on a buried fault will tend to slip left-laterally as the elliptical fault grows.

The field observations and model results favor the interpretation that the Hopena fault grew up from depth rather than down from the surface. A common pattern of surface deformation appears along the Hopena fault, other Koae faults, and faults in Iceland. The findings here thus are applicable to many faults.

1 Introduction

Normal faults are among the most prominent structures in the Earth's crust. For example, they form divergent plate boundaries (Pollard and Aydin, 1984). Since normal faults characteristically form where the crust is stretched thin, they play an important role in heat transfer through the crust. They also are sites of pronounced hydrothermal activity, especially at mid-ocean-ridges. Hydrothermal activity and mineralization account for a broad economic interest in normal faults. Normal faults also play a key role in creating sedimentary basins, and in both sealing and breaching hydrocarbon reservoirs. On volcanic islands, such as Hawai'i, normal faults contribute greatly to flank instability, which, in turn, may pose the threat of a tsunami to entire ocean basins (Cervelli et al, 2002). The origin and evolution of faults clearly affect a broad variety of important phenomena.

This study investigates faulting-related secondary features at the surface, e.g. opening mode fractures, to understand the growth of normal faults. Secondary fractures contribute to the mechanical linkage of previously discontinuous faults (Segall and Pollard, 1983; Martel and Boger, 1998) as well as the hydraulic linkage between segmented faults (Gudmundsson, 2000; National Academy of Sciences, 1996). Fault tipline conditions play important roles in the initiation and termination of earthquake ruptures, and secondary fractures in these regions potentially allow insight into fault slip behavior and may serve as precursors for co-seismic slip (King and Nábêlek, 1985). The central focus of this study is to relate the pattern of secondary fractures and other faulting-related deformation to the evolution of a normal fault that breaches the surface. Faults that breach the surface might originate either: (1) at the surface and grow down from it, or (2) at depth and grow up to the surface. Both growth models may yield distinct patterns of deformation during their evolution. This study investigates the differences between the two growth models and their congruence with the field data from one normal fault.

Normal faults have been proposed to nucleate at the surface nucleation in

Iceland, the East African Rift, and in Canyonlands National Park, Utah (Opheim and Gudmundsson, 1989; Acocella et al., 2003; Cartwright and Mansfield, 1998). Gudmundsson (1987) and Gudmundsson and Bäckström (1991) propose that normal faults form from vertical fractures at the surface but that as the faults propagate down their dip decreases. The studies by Gudmundsson and Bäckström (1991), Cartwright and Mansfield (1998), and Acocella et al. (2003) utilized detailed field data, but did not address the fault growth in light of mechanical consideration.

Growth of normal faults up from depth has been proposed based on studies of normal faults on the Big Island of Hawai'i (Langley, 2001) and on Iceland (Grant and Kattenhorn, 2004). Faults from both of these areas resemble the fault of this study. Both studies combined field examinations with two-dimensional mechanical analyses of normal faults to account for features removed from the ends of the faults. Neither of the studies addressed issues bearing on deformation at the ends of normal faults, lateral fault propagation, or the three-dimensional geometry of a normal fault.

This study addresses secondary structures near a normal fault and relates them to possible subsurface fault geometries. It exploits outstanding exposures along active normal faults growing in the Koae fault system on the Big Island of Hawai'i. The youth of the faults and their superb preservation permit additional insight into how normal faults grow. Systematic features along the faults include two belts of fractures, one on each side of the fault trace, a third belt of fractures along and past the fault scarp, and anticlinal buckles at the base of the fault scarp. Profiles across the fault scarp and past the scarp end reveal ground flexure that transitions from a breached monocline to a gentle unbreached monocline. The characteristics of these features provide valuable information about the complicated process of fault growth.

The study opens by describing the structures near the end of one of the faults in the Koae fault system - the Hopena fault (Figs. 1, 2). This is followed by elastic analyses of displacement and stress fields around a three-dimensional normal fault. Several subsurface geometries are used to investigate each growth model. The stress

fields prove to be useful in understanding the location, orientation, and the style of the observed structures along the fault. The interplay of numerical modeling and detailed field observations complement each other and shed light on the growth of normal faults.

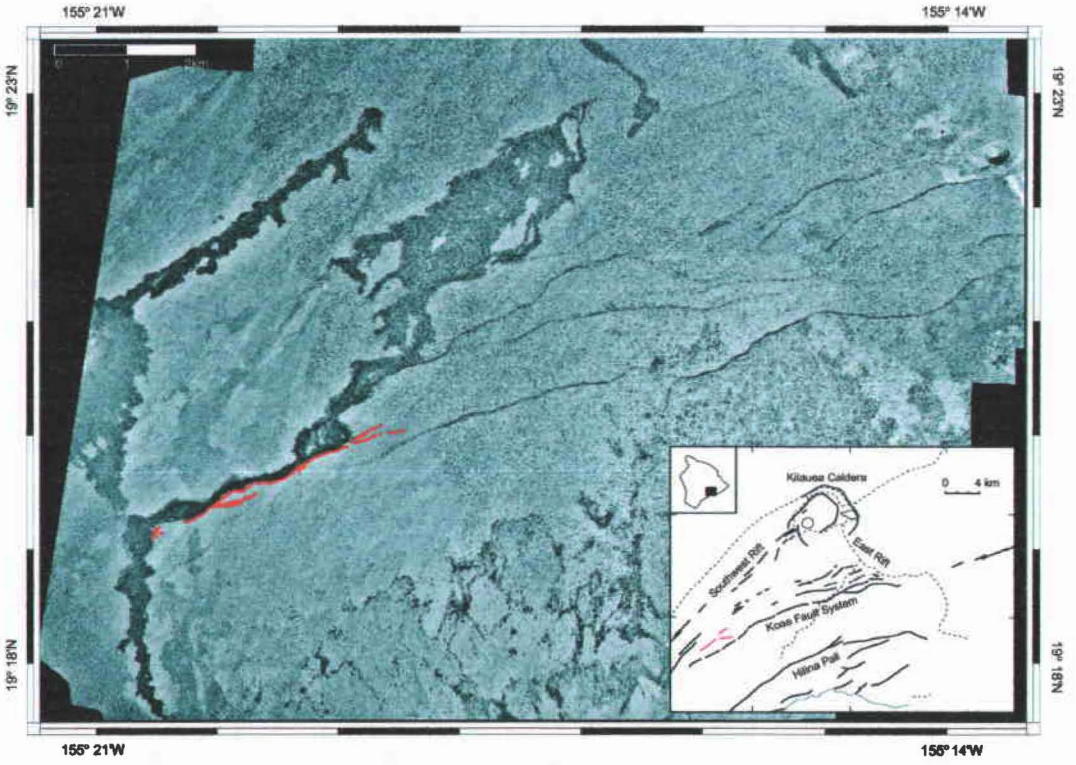

Figure 1: Orthorectified and georeferenced aerial photo map of the central and western Koae fault system, Big Island of Hawai'i, mapped at 1:45000, Photos taken in 1977. The Hopena fault is traced in red. The fault end mapped in detail in Fig.2 is the northwestern trace.

Figure 2: Next page: Structural map of the northern fork of the Hopena Fault.

North Fork of the Hopena Fault

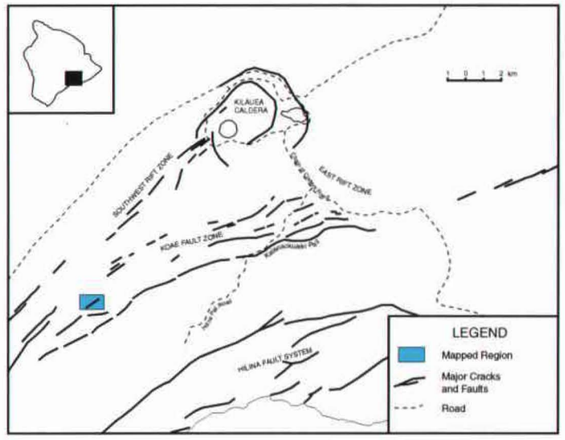

155°19'05" W
256500mE
155°18'45" W
257100mE
2139750mN
19°20'10" N
19°20'00" N
2139300mN

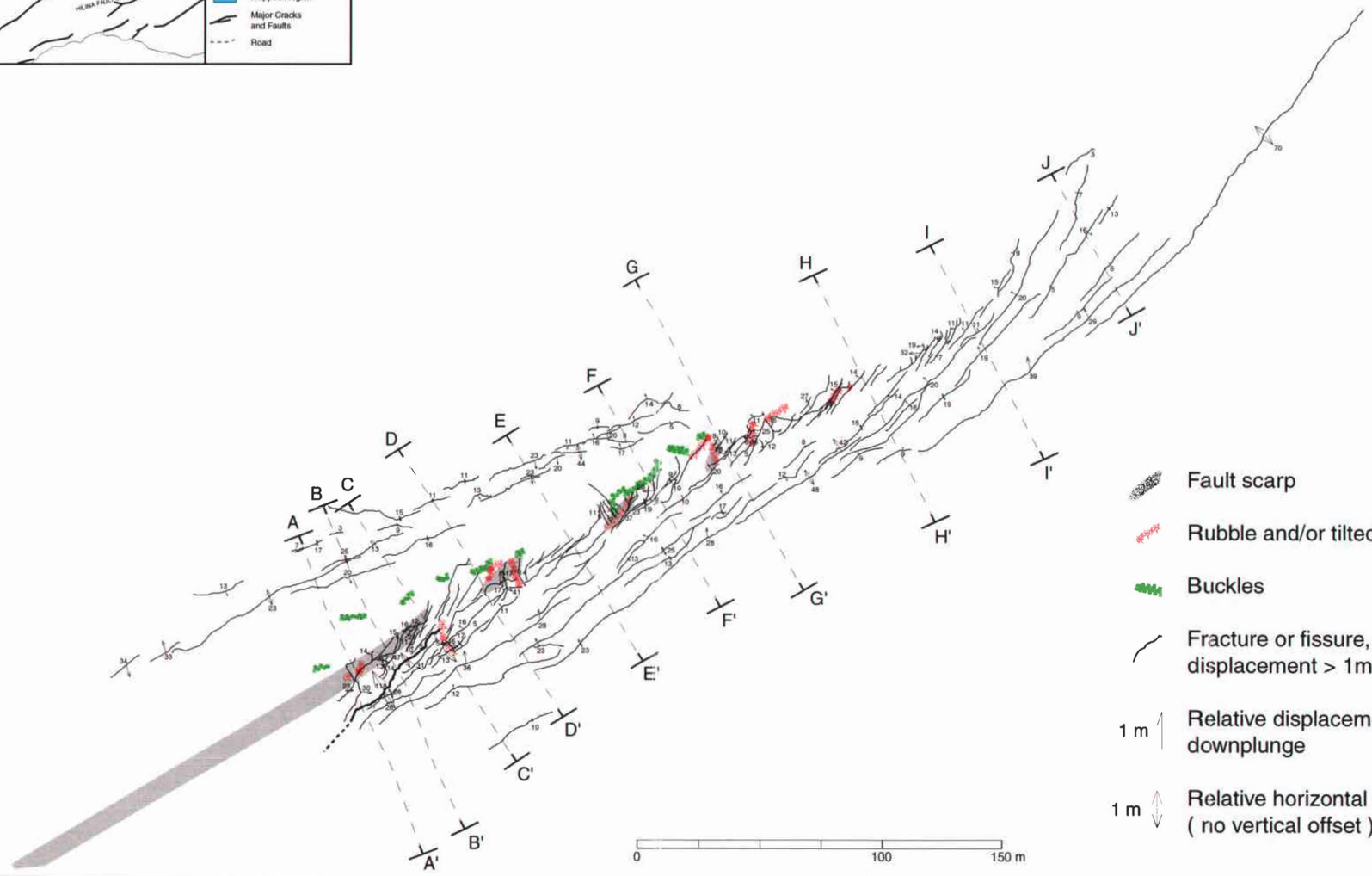

- Fault scarp
- Rubble and/or tilted slabs
- Buckles
- Fracture or fissure, thick line for displacement > 1m
- 1 m — Relative displacement pointing downplunge
- 1 m — Relative horizontal displacement (no vertical offset)

2 Field Observations

2.1 Koae Fault System

The Hopena fault is part of the Koae fault system (KFS) (Fig. 1), which traverses Kilauea's flank about 4km south of the caldera and lies between the east and southwest rift zones of Kilauea. The normal fault system is about 12km long and tapers in width westward from 3km to 1km. The Kalanaokuaiki fault marks the southernmost extent of the KFS. It is the longest of the KFS faults. The KFS faults generally dip to the north (Duffield, 1975). They feature fissures along the uplifted side, buckles right at the scarp bases (MacDonald, 1957), and fractures on the downdropped side.

Most of the area is draped by pahoehoe flows 400 to 750 years old (Wolfe and Morris, 1996) that dip gently to the south (Duffield, 1975). Lava flows a few decades old cover the ends of many faults in the eastern part of the KFS. A 1974 lava flow covered the western end of several faults in the KFS (Pollard et al, 1983), including the western end of the Hopena fault, but the eastern end was not covered. Structural details that are superbly displayed along the east end of the Hopena fault are obscured along most of the faults of the KFS. Also, unlike many faults in the KFS, which link with other faults, the eastern end of the Hopena fault is fairly well defined. This study focuses on the east end of the Hopena fault to take advantage of the exposures there.

2.2 Hopena Fault

Structures are abundant and diverse, and somewhat complicated along the trace of the northern fork of the Hopena fault (Fig. 2), but nonetheless they form systematic patterns. The patterns are described here from west to east.

The trace of the Hopena fault is $\sim$ 4km long and has an overall trend of S62°W (Fig. 1). At its eastern end the fault forks. The northern fork continues at the general

strike of the Hopena fault. The southern fork curves to the south, merging at an acute angle with the Kalanaokuaiki Fault. Vegetation is sparse in this portion of the KFS, and does not obscure the faults. Low-lying areas along the hangingwall side of the fault are covered by ash no thicker than 30cm. The detailed geometry of tectonic fractures and fissures is governed by cooling joints in basalt (MacDonald, 1957). In terms of the surface expression, the Hopena Fault appears representative of the Koae Faults, and the northern fork of its eastern end is exceptionally well preserved.

The scarp of the Hopena fault reaches a maximum height of 7-10m along the central portion of its trace and $\sim$ 6m at the northern fork. Rubble accumulates at the base of the scarp (Fig. 3). A series of profiles across the fault shows that the steep scarp gradually diminishes in height to the east (Fig. 4). These profiles reflect a fractured and faceted monocline with a steeply dipping central limb (Fig. 4 profile D-D'). In profiles A-C, the surface of the downthrown side slopes towards the fault trace. To the east of profile E-E', the throw of the fault decreases and the fractured surface is warped into a more gentle monocline. Throw is defined here as the maximum vertical distance between high- and low-points adjacent and on opposite sides of the fault scarp. Profile G-G' marks the eastern end of the fault scarp, here defined as where the throw drops to less than 1m and individual fractures accommodate dip-slip of less than 50cm. Further east, past the fault scarp, the monoclinal flexure becomes even gentler, throw diminishes to less than 1m, and dip-slip displacements are less than 10cm across the fractures on the monocline.

Three belts of fractures accompany the fault trace. One is located on the footwall (south side) of the fault, one along the fault scarp and to the east of it, and another on the hangingwall. The boundary between the footwall fissures and the scarp fractures commonly is indistinct, whereas the hangingwall fractures are distinct from the scarp fractures.

The fractures with the longest trace lengths and greatest apertures are on the footwall. One fracture gapes open more than 1m (Fig. 2). This gaping fracture is

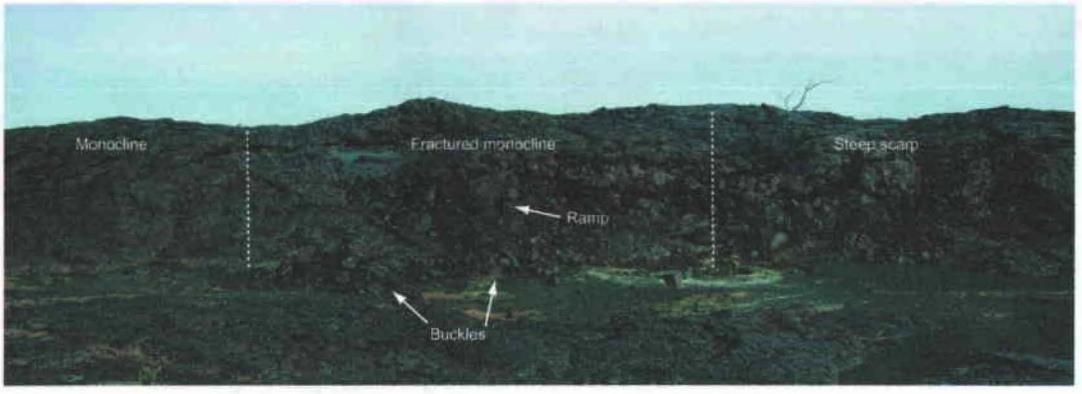

Figure 3: Photo taken from the north looking south onto the fault scarp of the Hopena fault. Proceeding from west (right) to east (left), the scarp gradually changes from a steep scarp to fractured monocline to a monoclinal flexure.

termed a fissure to distinguish it from the other fractures. Footwall fissures are a characteristic feature of all faults in the KFS. Fractures and fissures strike parallel to sub-parallel to the fault strike (Fig. 5). Along fractures and fissures on the footwall the relative displacements are almost purely opening mode (Fig. 6). To the east of the scarp, i.e. east of profile G-G', these fractures curve to the north, striking northeast rather than east-northeast.

A consistent pattern of right-stepping echelon fractures that strike northeast occurs along and past the scarp. The pattern is most complicated at the western end of the mapped fault scarp and becomes simpler to the east (Fig. 2). The fractures commonly are spaced 1-2m apart and divide the scarp into a series of northeast-trending ramps (Fig. 3). These ramps commonly are broken into blocks by smaller fractures with varying strikes. The relative horizontal displacement across the most prominent fractures is largely opening (Fig. 5, 6). Along most of the fractures the northern fracture walls are dropped down with respect to the southern walls. The length of the fractures decreases to the east of the scarp. The belt of fractures narrows east of profile H-H'. Many ends of individual fractures east of profile H-H' curve to the north. This belt ends just east of profile J-J'.

The kinematics of strike slip vary along these fractures. West of profile E-E' right-lateral slip occurs locally on some fractures but this slip is an order of magnitude smaller than the opening (Fig. 6). East of profile E-E' the character of the fractures changes. They still strike northeast but only a few show more than 50cm of dip-slip. Fractures that exhibit larger vertical offsets contain rubble that prevents accurate measurements of slip. The strike-slip along fractures between profiles E-E' through G-G' is left-lateral (Figs. 5, 6). The dip-slip displacement along individual fractures here does not exceed 10cm. The opening across these fractures is roughly equal to the strike-slip displacements across the fractures; strike-slip relative displacements are left-lateral (Figs. 5, 6).

On the hangingwall (Fig. 2), a narrow belt of fractures trends on average N73°E and merges with the eastern end of the fault scarp at an acute angle near profile G-G'. The relative displacement along these fractures is mainly opening (Figs. 5, 6). The apertures of these fractures are as large as 40cm. At the fracture ends the apertures drop to zero.

Near the base of the fault scarp, on the hanging-wall side of the fault, the ground surface is buckled into several sharply hinged anticlines (Figs. 2, 3, 4 profile F-F'). Some are fractured just at the hinge, others are highly fractured throughout. These buckles vary in length from 2-10m. They are generally 1-2m wide and 0.5-1m tall. The distance from the buckles to the base of the fault varies from 1-20m near profile B-B' and decreases to the east. The trends of the buckle fold axes are highly variable. Even within a single buckle, the fold axis trend can change from southeast to northeast. Near the eastern end of the fault scarp, buckles are only 1-4m north of the base of the scarp. Buckles do not occur east of the end of the fault scarp (Fig. 2).

The structures around the Hopena Fault resemble those mapped by Langley (2001) along the eastern end of the Ohale Fault located 3km northeast of the northern fork of the Hopena Fault. The broad surface deformation and general fracture patterns also mirror those along the western end of the Kalanaokuaiki fault.

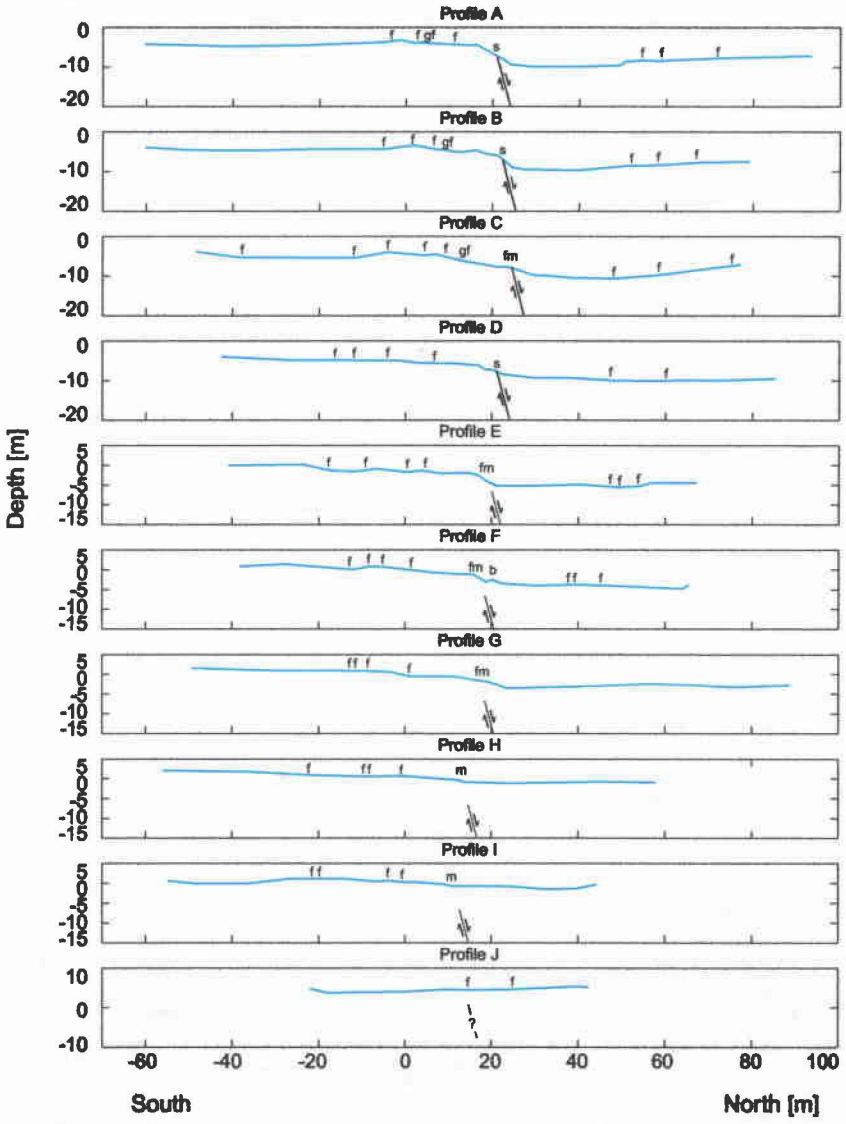

Figure 4: Topographic profiles across the North Fork of the Hopena Fault from west-south-west (top profile) to east-north-east (bottom profile). Profile locations are shown on Figure 2 (map). Faults are shown in solid lines where a scarp exists and dashed where inferred at depth. Labeled features: fractures (f), gaping fissures (gf), scarp (s), fractured monocline (fm), monocline (m), and buckles (b).

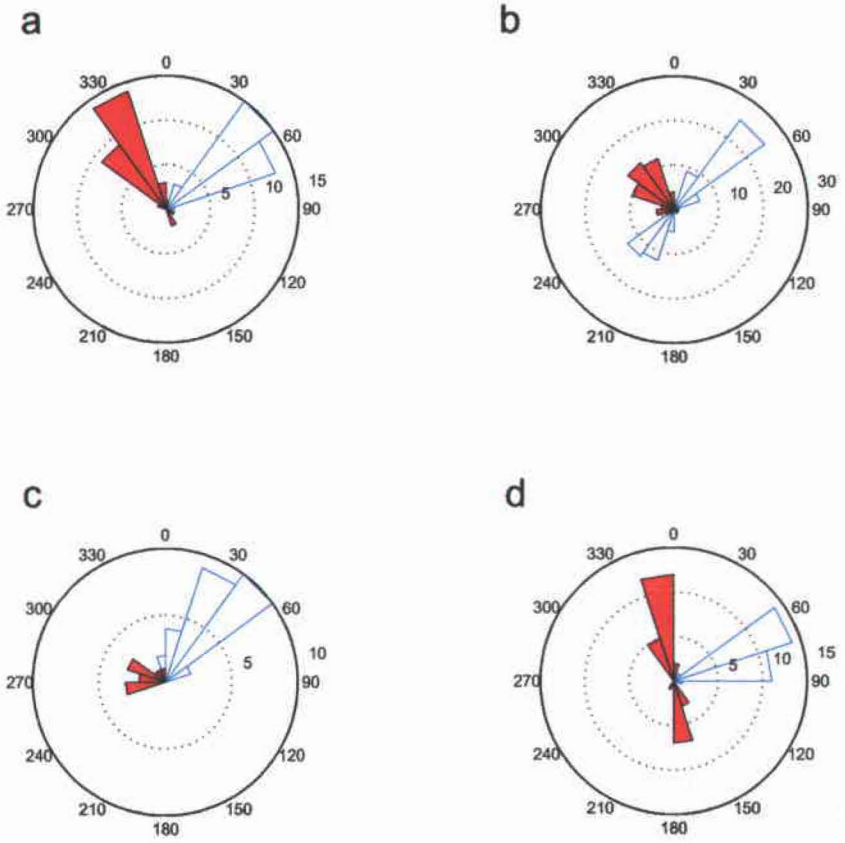

Figure 5: Radial histograms of fracture strike (unfilled sector) and trend of horizontal relative displacement (filled sector). Fracture strikes are 90° counterclockwise of the fracture dip direction. Horizontal displacements are measured in the direction from uplifted wall to downdropped wall. The size of the sectors indicates the number of fractures and number of displacement measurements in a range of orientations. (a) Fractures on the footwall. (b) Fractures at the scarp. (c) Fractures east of the scarp. (d) Fractures on the hangingwall.

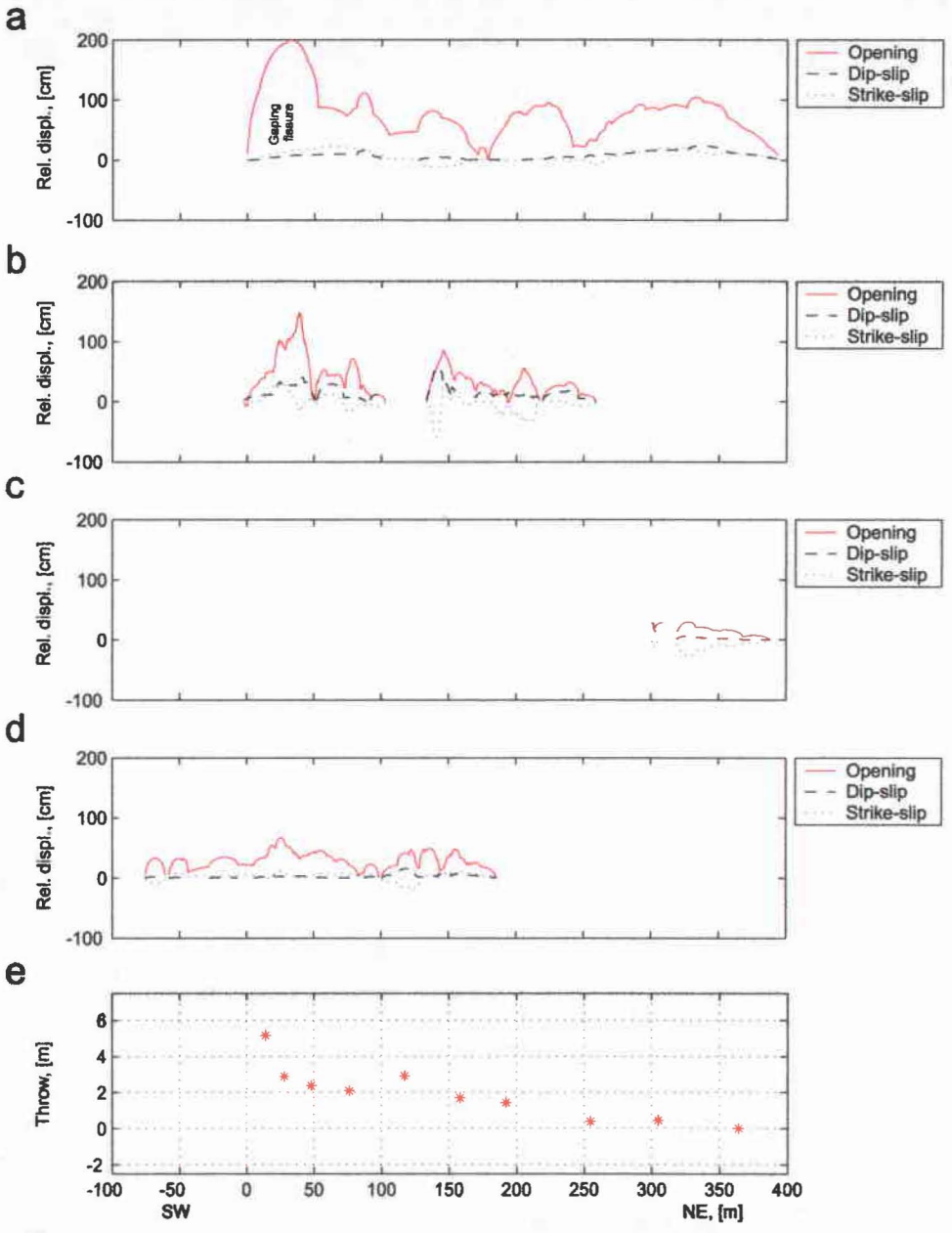

Figure 6: Relative displacements along subsets of fractures (a-d), and throw across the fault from fault profiles (e). All displacement measurement are projected onto a fault-parallel axis. The origin is set at the western end of the westernmost fractures on the footwall. Negative strike-slip values correspond to left-lateral strike-slip. (a) On the footwall. (b) At the scarp. (c) East of the scarp. (d) On the hangingwall. (e) Throw. The location of throw measurements indicates the intersection of profiles and fault scarp.

3 Mechanical Analysis of Near-Fault Deformation

The patterns of deformation along the northern fork of the Hopena fault appear characteristic of the Koae faults as a whole and may be characteristic of many normal faults in general. The goal now is to explain the process of deformation and, in particular, the fracturing, using mechanical models. I infer that the orientation of fractures that nucleate near the tip of the fault trace depend on the concentration of stresses near the fault tipline (e.g., Pollard et al., 1982; Cruikshank et al., 1991; Martel, 1997; Martel and Boger, 1998). The exact character of stress concentration near the tip in turn depends on the mode of slip on the fault itself. For a normal fault, such as the Hopena fault, the mode of slip along vertical portions of the tipline will be exclusively tipline parallel shearing, mode III (for modes see Fig. 7). Along horizontal portions of the tipline of a normal fault, slip will be purely tipline-normal sliding, mode II. Along other portions of the perimeter of a dip-slip fault a combination of the two modes will govern near-tip fracture nucleation. Different fault geometries thus should yield distinct patterns of fractures at the surface near the fault tip. The effects of different simple fault geometries are contrasted in this study.

3.1 Model Fault Geometry

Surface-breaching faults have been idealized as semicircular (Crider and Pollard, 1998) or rectangular (Grant and Kattenhorn, 2004). Three-dimensional data indicate that many normal faults in nature tend to have a roughly elliptical tipline shape (Rippon, 1985). Some normal faults that are vertically restricted by layering or the free surface assume shapes of truncated ellipses (Nicol et al., 1996). Here, truncated elliptical faults and rectangular faults are used to idealize faults that nucleate at the surface and grow down from it (Fig. 8a, b). Faults growing up from depth are idealized by a succession of different geometries: a full ellipse when blind, a full ellipse with its upper portion tangential to the ground surface at an intermediate stage, and

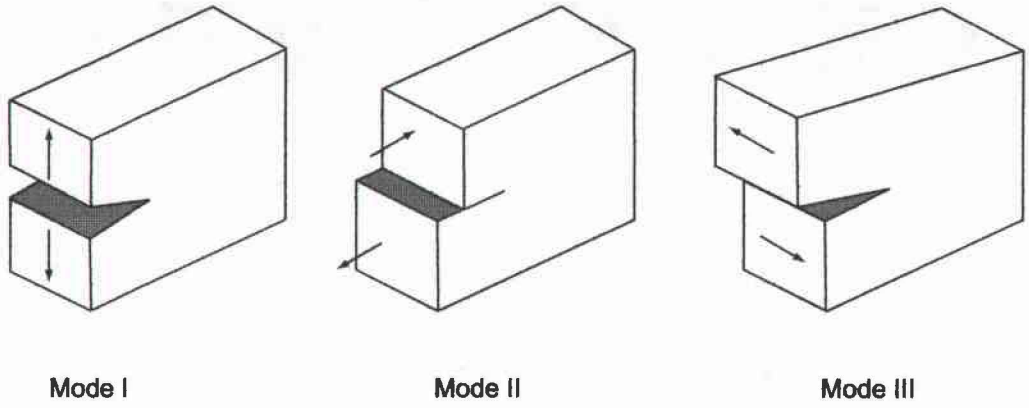

Figure 7: Fracture modes of fractures and faults. Mode I refers to opening of fractures, Mode II refers to tipline-normal sliding, Mode III refers to tipline parallel tearing.

finally a fault truncated by the surface (Fig. 9). Common aspect ratios of elliptical faults range from $\frac{b}{a} = \frac{1}{8}$ to $\frac{2}{1}$, where b is the down-dip semi axis length and a is the along strike semi axis length (Nicol et al., 1996). The analyses here consider planar elliptical and rectangular faults that have a constant aspect $\frac{b}{a}$ ratio of $\frac{1}{2}$. All faults dip at 75°; results of fault parameter inversions using topographic data favor this dip over dips of 65° or 85°.

The insets of figures 8a and 8b depict slip near half-elliptical and rectangular tipline geometries, respectively. These represent faults nucleated at the surface. Near the free surface, tipline-parallel sliding, mode III, dominates the slip on the half-elliptical fault and the rectangular fault. In fact, tipline-parallel sliding is the only mode of slip along the vertical portions of the tipline. The inset of figure 8c shows that dip-slip on the truncated elliptical fault is resolved into both tipline-parallel sliding (mode III) and tipline-normal shearing (mode II) components. The mode II and mode III components in Figs. 8a, b, and c clearly differ. The mechanical conditions induced by these different fault geometries are expected to cause different orientations of fractures near the fault tipline. The nature of fractures near the ends of faults should be able to shed light on the geometry of the tipline itself.

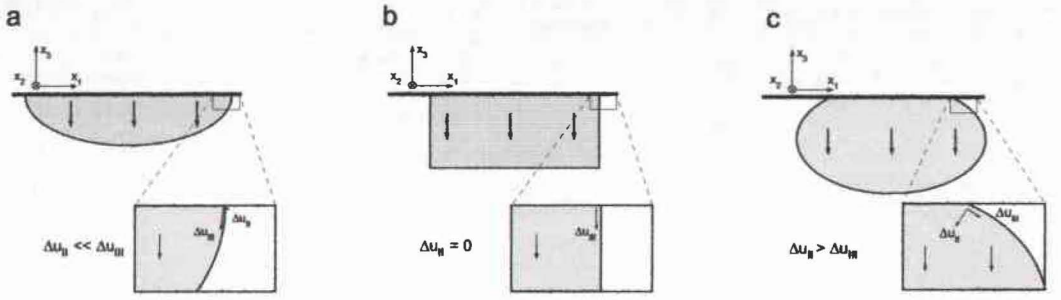

Figure 8: Model fault geometries. (a) Half-ellipse, (b) rectangle, and (c) truncated ellipse. Displacement discontinuities of modes II and III, tipline normal sliding and tipline parallel shearing, respectively, are shown in insets, where the fault intersects the surface.

3.2 Ambient Stress Field and Boundary Conditions

A realistic representation of the regional stress conditions is needed to reflect the geologic setting on the south flank of Kilauea. The ambient stresses are complicated, being influenced by the presence of Mauna Loa, the rift zones and the relatively unconfined southern flank of Kilauea. Mauna Loa serves as an abutment to the north. The ambient stresses probably vary in time also as dikes intrude along the rift zones and earthquakes occur (Rubin and Pollard, 1987; Lipman et al., 1985). I follow the suggestions of Swanson et al. (1976) and consider the south flank to be close to laterally unconstrained. Here, for simplicity, the horizontal stresses normal to the fault strike are considered to be zero. A constant compressive (negative) stress is assigned parallel to the fault strike, and the vertical normal stresses due to gravity vary linearly with depth. This representation of the ambient field is consistent with the orientation of the Koae faults and their sense of slip (Swanson et al., 1976). This is an idealization of a stress field that is acknowledged to be complicated.

The assignment of the ambient stress field and the resolution of tractions on boundary elements makes use of several coordinate axes systems (CAS). The notation x_i^g refers to the global reference system with x_1^g parallel to fault strike, x_2^g horizontal and perpendicular to fault strike, and x_3^g up (Fig. 10a). A local reference frame is

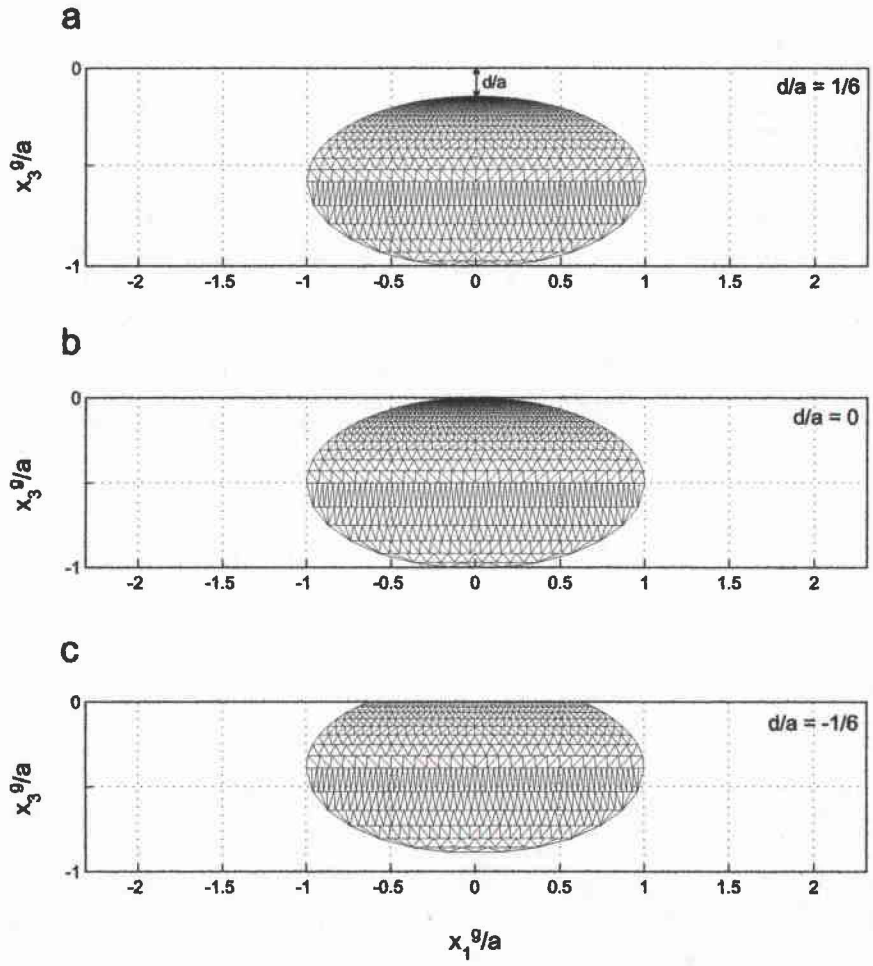

Figure 9: Discretization of blind ellipse (a) and intermediate full ellipse with its uppermost tipline tangential to the ground surface (b), and a truncated ellipse. The ratio $\frac{d}{a}$ is the normalized depth to the top of the fault. The $\frac{d}{a}$ ratio is positive for blind faults and negative for faults that breach the surface.

used as well (Fig. 10b). This reference frame, x_i^e, is used to assign tractions acting at the centers of the polygonal elements, has x_1^e pointing down-dip, x_2^e pointing along the strike of the element, and x_3^e pointing normal to the element plane and up.

A representation of the total stress field (Fig. 11) is achieved by superposing the perturbation associated with fault slip and the ambient stress field (Martel and Muller, 2000). The ambient stress field is represented by a vertical compressive stress that increases linearly in the $-x_3^g$ direction and a constant compressive stress assigned parallel to the fault strike:

$$\sigma_{33}^g = \rho\, g\, x_3^g \tag{1}$$

$$\sigma_{22}^g = -1MPa \tag{2}$$

$$\sigma_{11}^g = 0. \tag{3}$$

All other components of σ_{ij}^g are equal to zero. In the above equations g is the gravitational acceleration, ρ is rock density, ν is Poisson's ratio. Values of the material parameters are $\rho = 2700\ kg \cdot m^{-3}$, $\nu = \frac{1}{4}$, and E (Young's modulus) = 5000MPa (Langley, 2001).

All fault elements are kept from opening or interpenetrating by prescribing a Burger's vector component, b_3^e of zero at each element center. A complete shear stress drop is assumed on the entire fault plane. This maximizes slip and yields the maximum stress perturbation in the surrounding rock. The result here thus serves as an end member. To account for the effects of gravity and achieve a complete shear stress drop on the fault plane, the negative of the resolved gravity-induced traction, t_1^e, is prescribed at the center of each element comprising the fault plane. The tractions on the fault elements are calculated using Cauchy's formula (Lai et al., 1993):

$$b_3^e = 0 \tag{4}$$

$$t_1^e = \rho\, g\, x_3^g\, cos(\delta)\, sin(\delta) \tag{5}$$

$$t_2^e = 0, \tag{6}$$

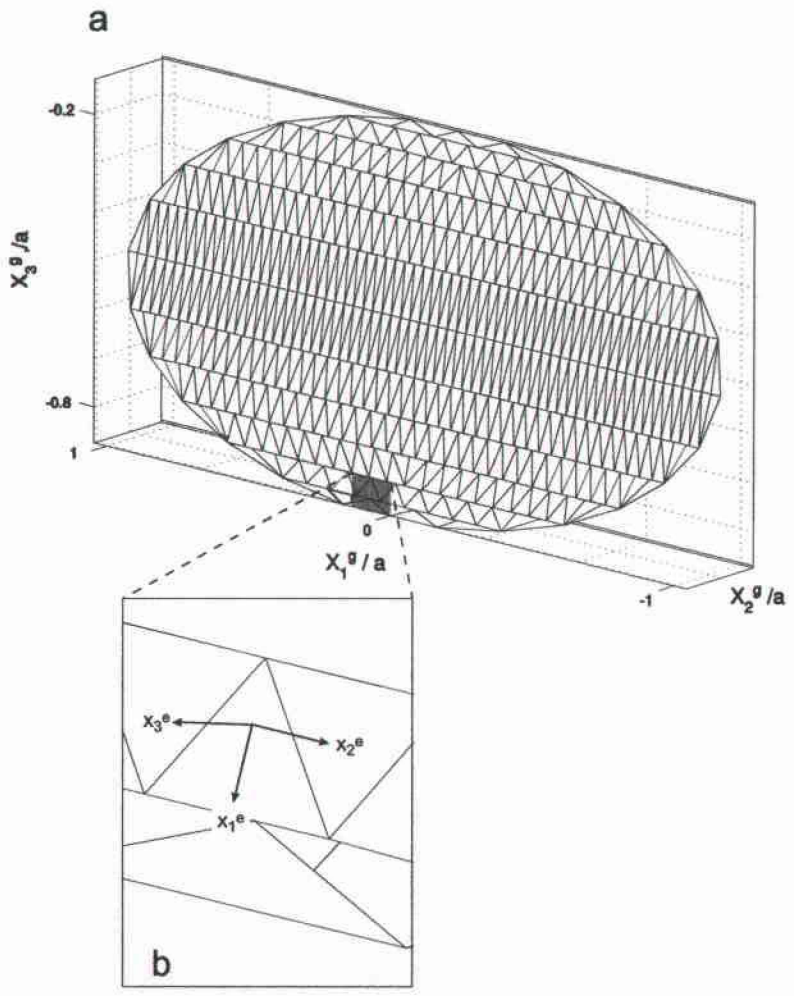

Figure 10: Discretized elliptical fault with (a) global CAS, and (b) a local element CAS. x_1^e points down dip, x_2^e points along the strike of the fault, x_3^e is normal to the fault plane and up.

where δ is the dip of the fault (75°). The boundary conditions in equations (4)-(6) are associated with the perturbation due to fault slip and reflect the central box depicted in figure 11. Superposed on the perturbation is the ambient stress field (equations (1)-(3)).

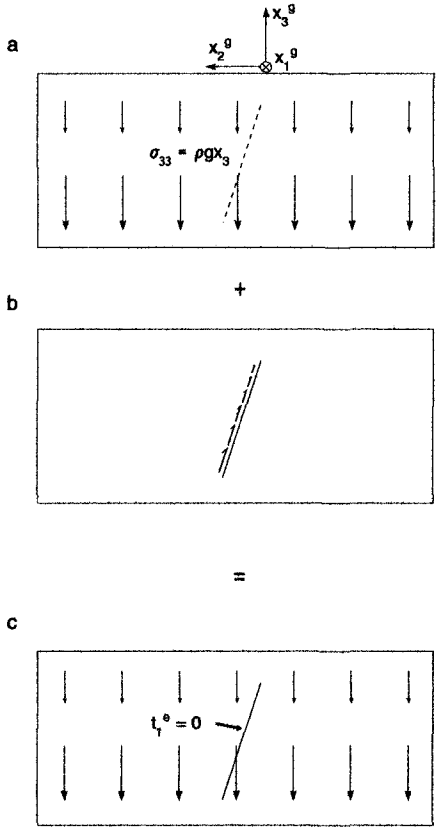

Figure 11: Cross-section views perpendicular to fault strike showing contributions to the stress field near a normal fault. (a) The ambient stress field is governed by gravity. (b) Perturbation due to the negative of shear tractions induced by gravity. (c) The superposition of (a) and (b) yields the total stress field around a fault without shear tractions.

3.3 Boundary Element Method

The analyses are carried out by utilizing Poly3D, a three-dimensional boundary element method (BEM) numerical code (Thomas, 1993). In this method, the

fault or fracture surface is divided into contiguous polygonal elements, each of which accommodates a constant amount of relative displacement. The displacement discontinuities across all elements are found by solving a system of linear equations that describes the influence of the elements on one another and that simultaneously satisfies the given boundary conditions. The boundary element solutions satisfy the governing partial differential equations for linear elasticity in a half-space. The domain requires no discretization and the number of linear equations solved is smaller than for other numerical techniques for solving partial differential equations such as finite element methods (Crouch and Starfield, 1983). Poly3D allows two types of boundary conditions to be specified at the center of each element: Burger's vector components or tractions (tension is positive). The code calculates displacements and the local stress tensor at points on a defined observation grid. A limitation of this routine is that Poly3D calculates the stress and displacement field for a single slip event, but cannot include the effects of previous slip events on the surrounding material. Tests on simple fault shapes for which analytical solutions exist show that Poly3d reproduces analytical results to within a few percent (Crider and Pollard, 1998).

3.4 Results

Two scenarios exist for the growth of the Koae faults: (1) the faults may have nucleated at the surface and grown radially down and laterally, or (2) they may have grown up from depth and breached the surface. To address these alternatives in the mechanical analyses, I model the stresses and displacements for several fault geometries. The field observations are of deformation and structures at the surface, and my working hypothesis is that the style, location, and orientation of the deformation and surface structures may be predicted based on the stress field at the surface. I begin by examining surface warping and then proceed to surface structures from south to north across the fault. The particular surface structures that I focus on are the footwall fissures, the fault scarp fractures, the hangingwall fractures, and the hangingwall

buckles. I evaluate the stress field for faults of increasing size to gain insight into how the surface structures develop and evolve as a fault grows.

Fractures and fissures are likely to form where tensile stresses are high. The trajectories normal to the most tensile stress in map view are a proxy for the strike of secondary fractures. Similarly, areas of large compressive stress indicate possible locations of buckles. Trajectories normal to the most compressive stresses serve as a proxy for the trend of the buckles. The analyses open by evaluating the stress and displacement fields for faults that nucleate at the surface. Two fault geometries are addressed: a lower half-elliptical tipline and a rectangular tipline. Analyses for these geometries are compared to those for a single elliptical fault at depth. Subsequent analyses account explicitly for the presence of a fault that breaches the surface and for fractures on the footwall and hangingwall.

3.4.1 Downward Growth

The vertical displacement field at the surface associated with half-elliptical and rectangular faults has a pronounced discontinuity where the model fault intersects the surface, at $x_2^g/a = 0$ (Fig. 12). In both cases, the displacements are largest where the faults intersect the surface, and they decay with distance from the fault. Past the ends of the model fault traces, the ground flexure is minimal.

The most tensile stress field is decidedly heterogeneous (Fig. 13b, e). Tensile stress concentrations are confined near the ends of the fault trace for both model fault geometries, but are most pronounced for the rectangular fault. To either side of the fault trace, however, the most tensile stresses are in fact compressive. Trajectories normal to σ_1 vary little between the two geometries. On the footwall of both faults trajectories normal to the most tensile stress are oblique to the fault strike. Past the fault trace end, still on the footwall, trajectories normal to the most tensile stress parallel the fault strike. On the entire hangingwall of the elliptical fault, trajectories normal to σ_1 are roughly parallel to the fault strike. On the hangingwall of the

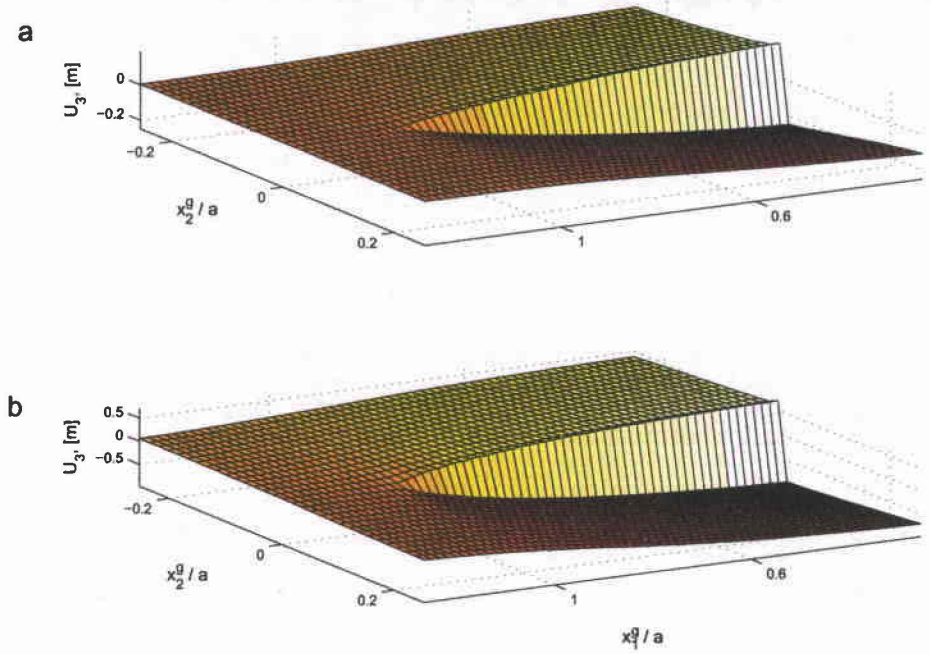

Figure 12: Oblique view of vertical surface displacements for (a) a half-elliptical, and (b) rectangular surface breaching fault. The observation plane is in the $x_1^g - x_2^g$ plane at $x_3^g = 0$.

rectangular fault, trajectories normal to σ_1 range from oblique to normal to fault strike along the fault trace. Past the fault trace on the hangingwall of the rectangular fault, trajectories normal to σ_1 range from oblique to parallel to the fault strike.

The magnitudes of most compressive stress are more uniform (Fig. 13c, f). The trajectories normal to the most compressive stress are perpendicular to the most tensile stress.

These analyses reveal that the two geometries produce similar effects in terms of displacements and stresses. Neither displacement field produces a breached monocline like the one observed along the Hopena fault. Along the fault trace on the model footwall, tensile stresses are parallel to the fault strike (Fig. 13b, e); this is inconsistent with the observed fractures and fissures that strike parallel to the Hopena fault.

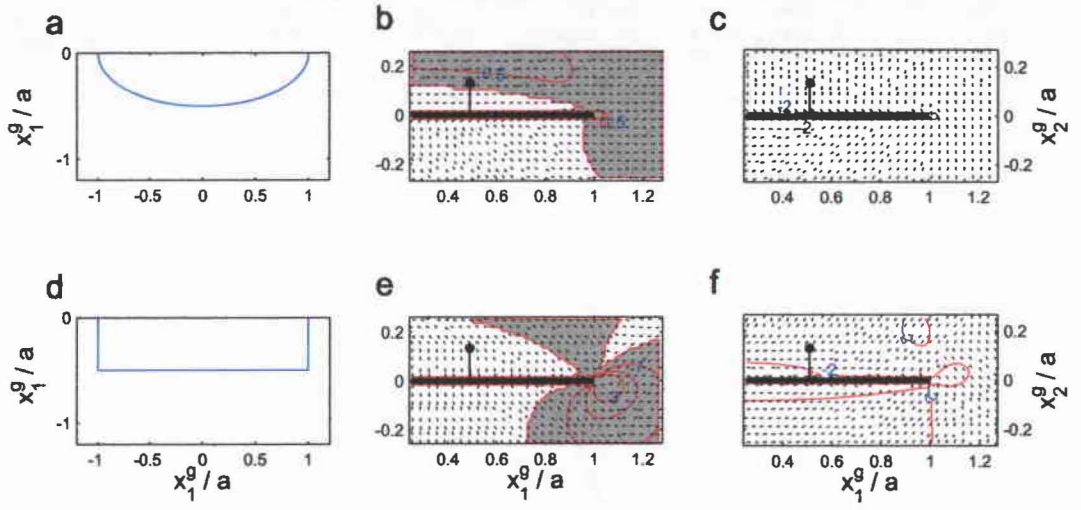

Figure 13: Maps of stress fields at the surface. The left column shows the fault geometry for each row. Fault scarps are indicated by a heavy line. The middle column shows magnitudes of the most tensile stresses, (σ_1), and orientations of possible fractures (trajectories are perpendicular to σ_1). The right column shows magnitudes of the most compressive stress, (σ_3), and orientations of possible buckle (trajectories are perpendicular to σ_3). Gray regions indicate tensile σ_1. The ball is on the downdropped hangingwall of the fault.

Along the fault trace on the hangingwall, the tensile stresses are weak and thus do not make for a compelling explanation of the belt of hangingwall fractures observed. Finally, although compressive stresses occur right at the fault trace on the hangingwall, the magnitudes also are low and do not require buckling (Langley, 2001). Thus the buckles at the base of the Hopena fault scarp are not readily explained by these models. The inconsistency of model predictions with the key observations allows me to reject the model that the Hopena fault nucleated at the surface and grew down. This prompts consideration of the alternative that the fault grew up from depth.

3.4.2 Upward Growth

The displacement and stress fields associated with a succession of fault geometries are tested here to investigate whether the Hopena fault may have nucleated at depth and grown up to the surface. A possible succession (Fig. 9) is represented by an elliptical blind fault, an elliptical fault with its upper tip tangential to the ground surface, and a truncated elliptical fault. Locations near the trace ends of breached faults at any particular stage would experience different displacement and stress fields as the fault grows.

Model results of vertical surface displacement indicate a smooth monocline above a blind fault (Figs. 14a, b). Vertical displacements are largest above the center of the blind fault and decrease gently towards the ends. Once the fault breaches the surface, vertical displacements are discontinuous where the fault intersects the free surface (Fig. 14c), and monoclinal flexure past the end of the model fault trace dies out a short distance from the end, similar to the case in Fig. 12.

For a blind fault, the greatest tensile stress concentration is on the footwall a short distance from where the fault projects to the surface, between $-0.1 \leq x_2^g/a \leq 0$ (Fig. 15b). The trajectories normal to the most tensile stress parallel fault strike. The greatest compressive stress concentration is on the hangingwall close to $x_2^g/a = 0$ (Fig. 15c). Along $x_2^g/a = 0$, where the blind fault projects up to the surface, the transition from areas of tensile to compressive stress concentration is marked by a transition in directions of principal stresses as well. Trajectories perpendicular to the most tensile stress change from being fault-parallel on the footwall, to trending obliquely along $x_2^g/a = 0$, to being either fault-normal or vertical on the hangingwall. Tensile and compressive stress concentrations increase the closer the fault tipline is to the surface.

The surficial stress pattern changes drastically once the fault breaches the surface (Fig. 15e, f, h, i). Surface stress concentrations shift towards the ends of the fault scarp. Along the fault scarp, away from the ends, stress concentrations

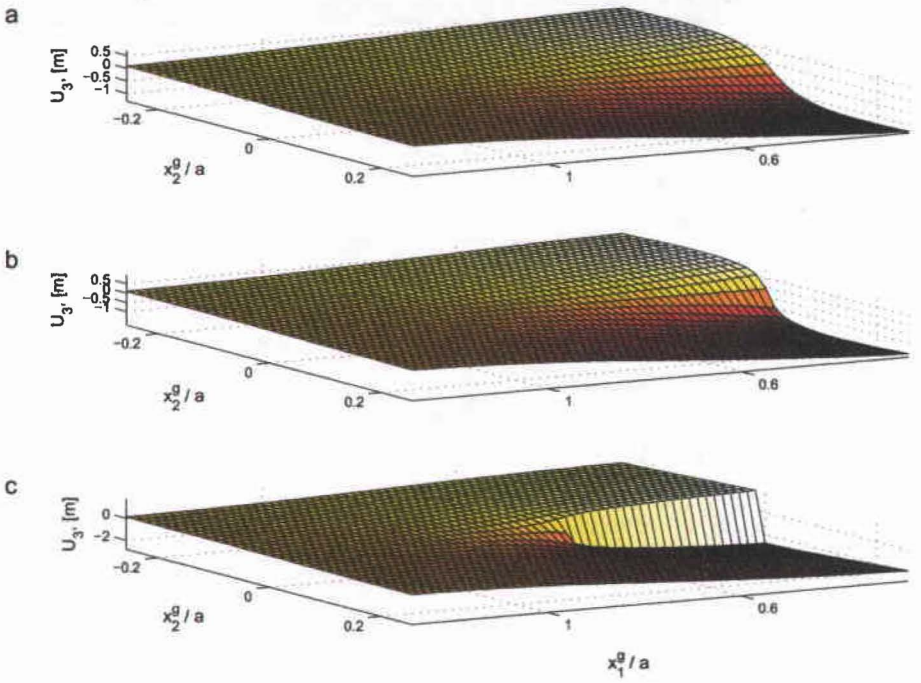

Figure 14: Oblique view of vertical surface displacements for an isolated fault. (a) For a fault with upper tip at 50m. (b) For a fault with the upper tip tangential to the observation plane. (c) For a breached fault. The observation plane is in the $x_1^g - x_2^g$ plane at $x_3^g = 0$. See Fig. 9 for the corresponding fault geometries.

vanish. On the footwall, the orientation of the most tensile stresses along the scarp are vertical (Fig. 15h), whereas above blind faults, the stresses normal to the fault scarp are tensile (Fig. 15b). Right at the fault trace ends trajectories perpendicular to σ_1 are fault-normal (Fig. 15h). Further past the scarp end, between $0.7 \leq x_2^g/a \leq 0.9$, the orientations of principal stresses are similar to those above blind fault.

The model results lead straightforwardly to predictions of secondary structures that might form. Fractures that may open above a blind fault along the developing monoclinal, central limb (i.e., near $x_2^g/a = 0$) would tend to strike obliquely to the fault strike (Fig. 15a,d, 16a,b). Once a fault breaches the surface the principal stresses rotate such that new fractures would tend to strike roughly perpendicular to the fault

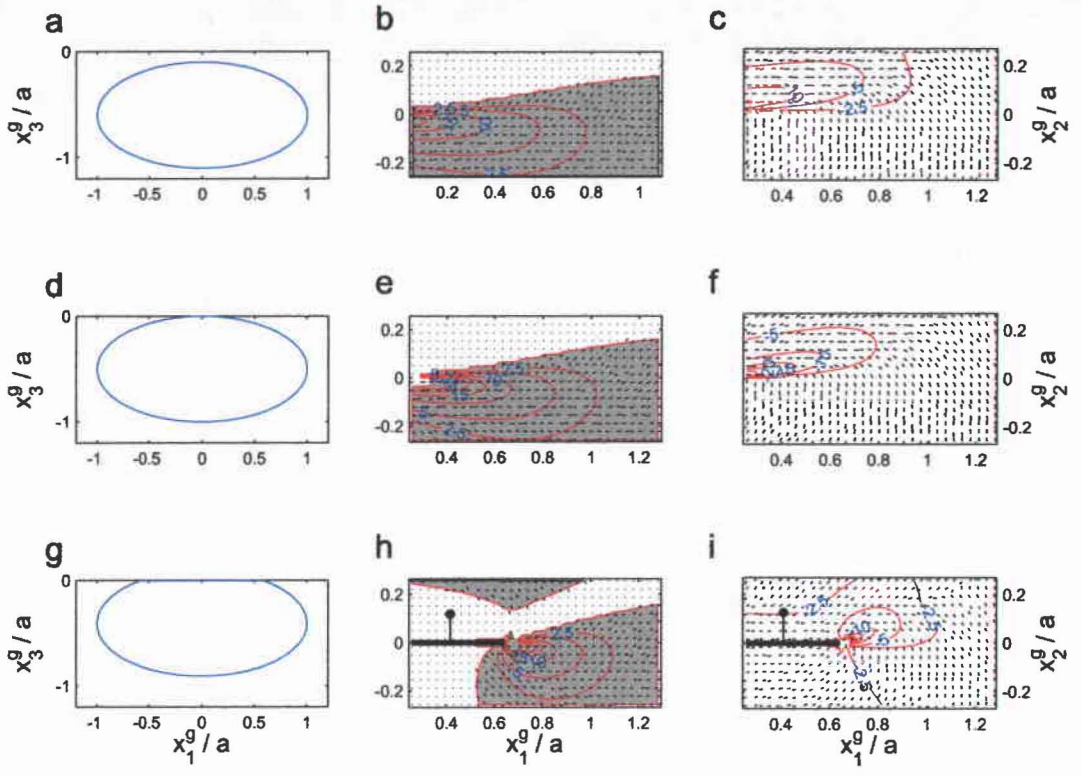

Figure 15: Geometry of faults and maps of stress fields at the surface near an isolated fault. The left column shows the fault geometry and position for each row. The center column shows magnitudes of the most tensile stresses, (σ_1), and orientations of possible fractures (trajectories are perpendicular to σ_1). The right column shows magnitudes of the most compressive stress, (σ_3), and orientations of possible buckle (trajectories are perpendicular to σ_3). Gray regions indicate tensile σ_1. Dotted trajectories of principal stress indicate where stress trajectories are vertical. Traces of breached fault are indicated by a heavy line. The ball is on the downdropped side of the fault.

strike (Fig. 16c). Along a pre-existing fracture oblique to the fault, however, the rotation of stresses would induce left-lateral slip.

The analysis results for a fault that grows up from depth account for several key observations. Model results of vertical displacements above blind faults reproduce the monoclinal flexure of the ground surface near the eastern end of the Hopena fault (Fig. 14). Even after the fault breaches the surface, monoclinal flexure occurs near

the end of the fault trace. The character of the most tensile stress concentration above blind faults is consistent with the location and orientation of fractures and fissures on the footwall of the Hopena fault. The model predicts that fractures can open over a large area on the footwall, and would strike parallel to the fault (Fig. 15). Directly above the fault tipline, the fractures that open would strike obliquely to the fault (Fig. 16a). The belt of echelon fractures at and to the east of the Hopena fault scarp thus can be accounted for by the model results (Fig. 15). The model results suggest that fractures on the footwall and scarp could form contemporaneously and field observations in nearly every case show that neither set of fractures occurs without the other. Left-lateral slip on preexisting fractures along $x_2^g/a = 0$ induced by a rotation of stresses is consistent with the observed relative displacements across fractures past the end of the Hopena fault scarp (Fig. 16). For blind faults with shallow tips, magnitudes and trajectories of σ_3 indicate that fault-parallel buckles may develop on the hangingwall close to $x_2^g = 0$ (Fig. 15c). This too is consistent with the locations of buckles near the Hopena fault.

A fault growing up from depth explains the surface warping, fractures and fissures on the footwall, echelon fractures at and to the east of the scarp, relative displacements across fractures east of the scarp, and the formation of buckles. The monoclinal flexure, fissures on the footwall, and formation of buckles are consistent with the two-dimensional modeling results of Langley (2001). His two-dimensional results, however, did not and could not account for the echelon fractures along the scarp and relative displacement across them.

The model results raise one key paradox though. Fractures that may open on the footwall when the fault is blind would tend to close once the fault breached the surface as fault-normal compressive stresses dominate the footwall. Langley (2001) postulated that the fissures on the footwall are kept from closing by debris stoped from the fissure walls. Guided by the field observations, the results from the isolated model fault here and the analyses of Langley (2001), an open fissure is included into

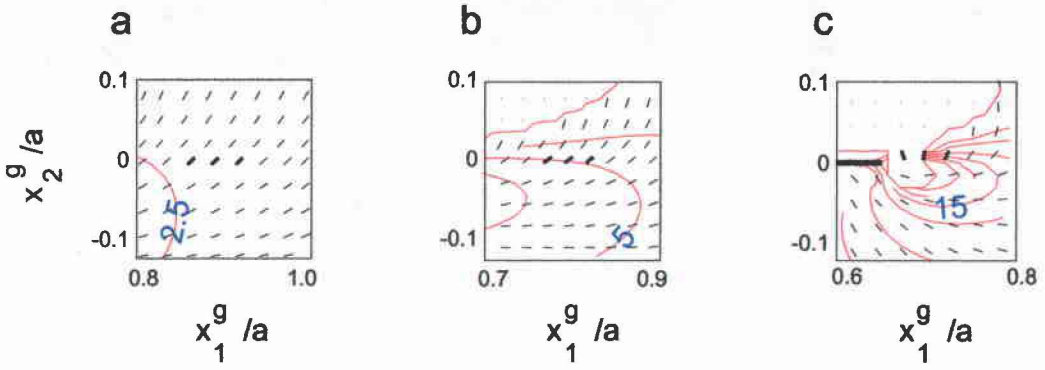

Figure 16: Map view of tensile principal stresses, (σ_1), and orientations of possible fractures near $x_2^g/a = 0$. Thick trajectories indicate a subset of fractures that are representative of fractures near the scarp for faults at different depths. (a) Blind fault with its upper tip at a depth of 50m, (b) fault with the upper tip tangential to the free surface, (c) for a breached fault.

subsequent model runs. The fissure is represented by the lower half of an ellipse centered at x_2^g = -25m. The fissure is 2.5km long and extends from the surface to a depth of 200m. Stress fields in vertical planes reveal that tension on the footwall prevails as deep as the upper tip of the fault itself even for faults with upper tips at depths greater than 200m (Langley, 2001). The dimensions and location are consistent with the length of the fissure and spacing between the fissure and Hopena fault. The fissure is kept from closing by prescribing an opening mode relative displacement, ($b_3^e > 0$) and its walls are set to be free of any shear tractions, ($t_1^e = t_2^e = 0$). The opening prescribed on the model fissure is consistent with $\sim$ 1.4m maximum aperture of the fissure near the Hopena fault.

Model results for a fault with a nearby fissure resemble those for an isolated fault. The similarities are apparent for both the vertical displacements (compare Figs. 14 and 17), and the stress fields (compare Figs. 15 and 18). For blind faults tensile stresses continue to dominate the footwall (Fig. 18a) and compressive stresses dominate the hangingwall (Fig. 18b). Between the fissure and $x_2^g = 0$, trajectories

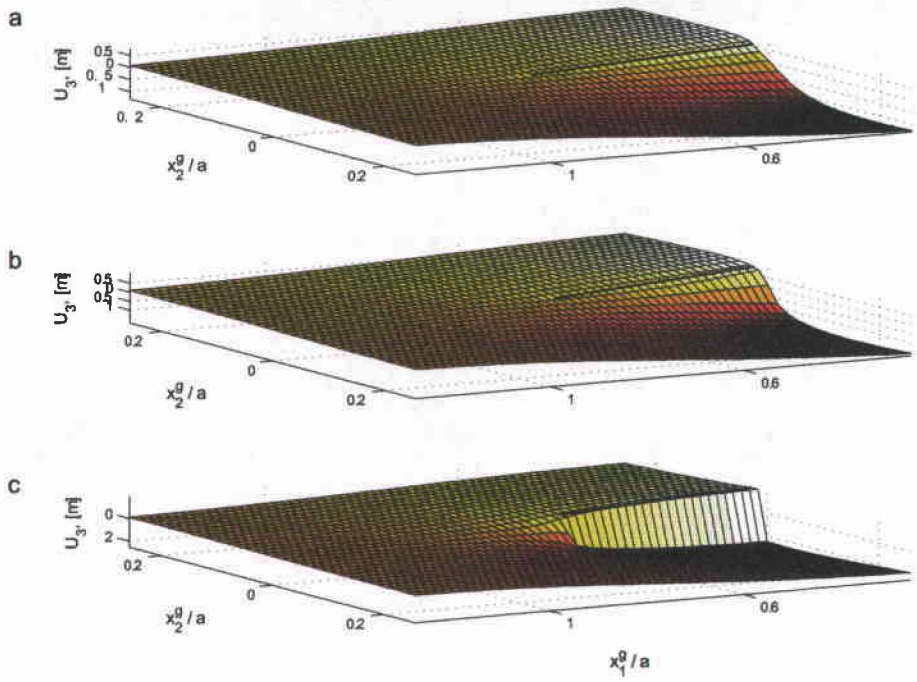

Figure 17: Oblique view of vertical surface displacements for a fault with nearby fissure. (a) for a fault with upper tip at $50m$, (b) for a fault with the upper tip tangential to the observation plane. (c) for a breached fault. The observation plane is in the $x_1^g - x_2^g$ plane at $x_3^g = 0$. The thick solid line indicates the trace of the vertical fissure.

perpendicular to σ_1 (Fig. 18c) have similar orientations to those for isolated blind faults (Fig. 15b). A careful comparison of Figs. 15c, f and 18c, f near $x_1^g/a = 0, x_2^g/a = 0$ reveals that magnitudes of the most compressive stresses on the hangingwall increase with the presence of the fissure. As was the case for the isolated fault, the stress patterns changes drastically once the fault breaches the surface (Figs. 18h, i). Stress concentrations focus near the end of the fault trace. The rotation of stress orientations during the successive stages of faulting also is similar to that for the isolated fault. Thus, the sense of relative displacement on preexisting echelon fractures along the scarp will still tend to be left-lateral.

The model containing a fault and nearby footwall fissure reproduce the surface

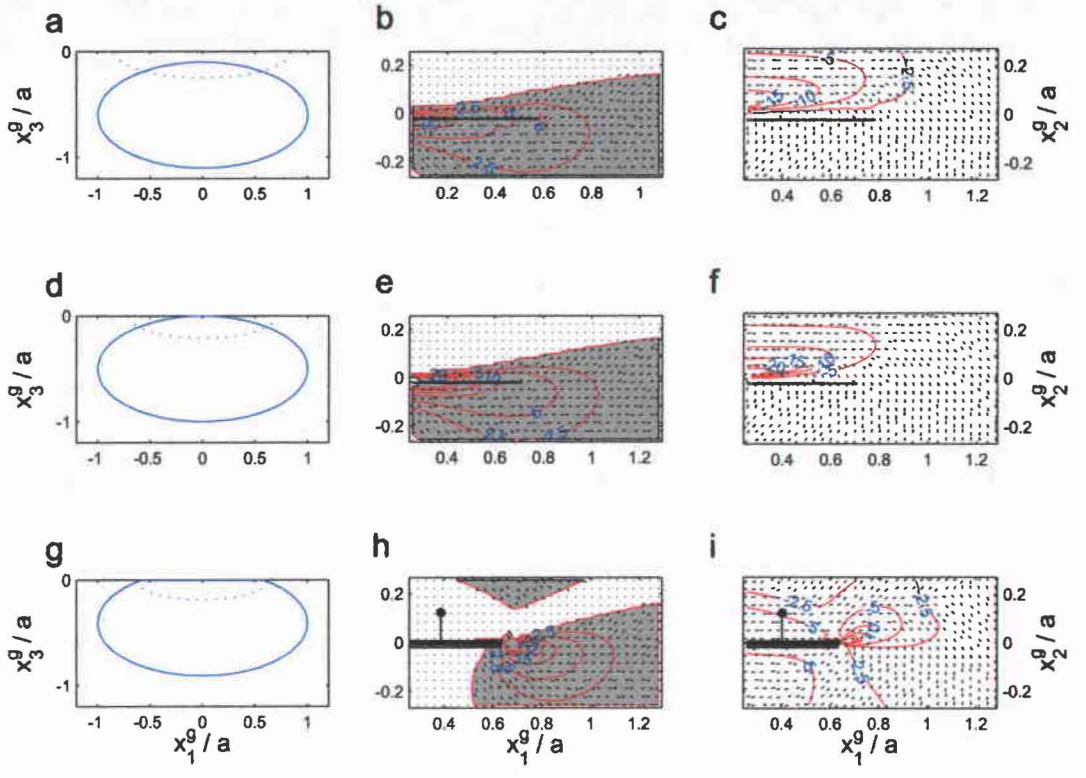

Figure 18: Geometry of faults and fissures and maps of stress fields at the surface due to a fault and fissure. The left column shows the fault geometry and position for each row. The location of the fissure is indicated by the dotted line. The center column shows magnitudes of the most tensile stresses, (σ_1), and orientations of possible fractures (trajectories are perpendicular to σ_1). The right column shows magnitudes of the most compressive stress, (σ_3), and orientations of possible buckles (trajectories are perpendicular to σ_3). Gray regions indicate tensile σ_1. Dotted trajectories of principal stress indicate where stress trajectories are vertical. Traces of the breached fault are indicated by a heavy line. The ball is on the downdropped side of the fault. The fissure traces are indicated by a medium line; this line is obscured by the fault in the bottom row.

warping, footwall fractures, echelon fracture pattern near the scarp, the sense of relative displacement at scarp fractures, and the formation of buckles near the scarp. However, the tendency for buckles to form at the base of the scarp is increased by the presence of the fissure, as previously noted by Langley (2001). The results from

the model fault with a nearby fissure, however, still do not account for fault-normal tension on the hangingwall which could promote the formation of a belt of fractures similar to the one observed along the Hopena fault. The lack of an explanation for these fractures requires further investigation of faulting related features at the northern fork of the Hopena fault.

The analyses of features observed at the surface do not account for the hangingwall fractures, which motivates an analyses of features that can be inferred to exist in the subsurface. Models of blind faults and of blind faults with a footwall fissure predict large tensile stress concentrations, and hence fracturing, near the upper tipline of the fault on the hangingwall in the subsurface (Fig. 19). The trajectories of principal stresses there indicate that secondary fractures at the upper tipline would strike parallel to the fault and dip roughly perpendicular to the fault (Fig. 19). These findings prompt a second modification to the model for a fault growing up from depth: an antithetic fracture is included as a traction-free half-ellipse extending over 80%, or $\sim$1.3km, of the length of the fault near the upper tipline. The upper tip of the antithetic fracture is at roughly the same depth as the upper tip of the fault is. This single model fracture represents what could be a series of fractures along a real fault. In the subsequent analyses, surface stresses are evaluated for a fault tip at very shallow depth, 15m, as the influence of the inferred antithetic structure on the surface only becomes apparent when the fault tip and the antithetic structure are near the surface (Fig. 20).

A large tensile stress concentration arises on the hangingwall close to the upper tip of the antithetic fracture (Fig. 21). Trajectories perpendicular to σ_1 indicate orientations of possible fractures parallel to the fault. Between the center of the fault and the fault ends the magnitude of σ_1 decreases and the trajectories perpendicular to σ_1 bend subtly but distinctly towards the fault (see stippled region in Fig. 21).

Model results that account for an antithetic fracture at shallow depth yield locations and orientations of tensile stresses that are consistent with the orientation

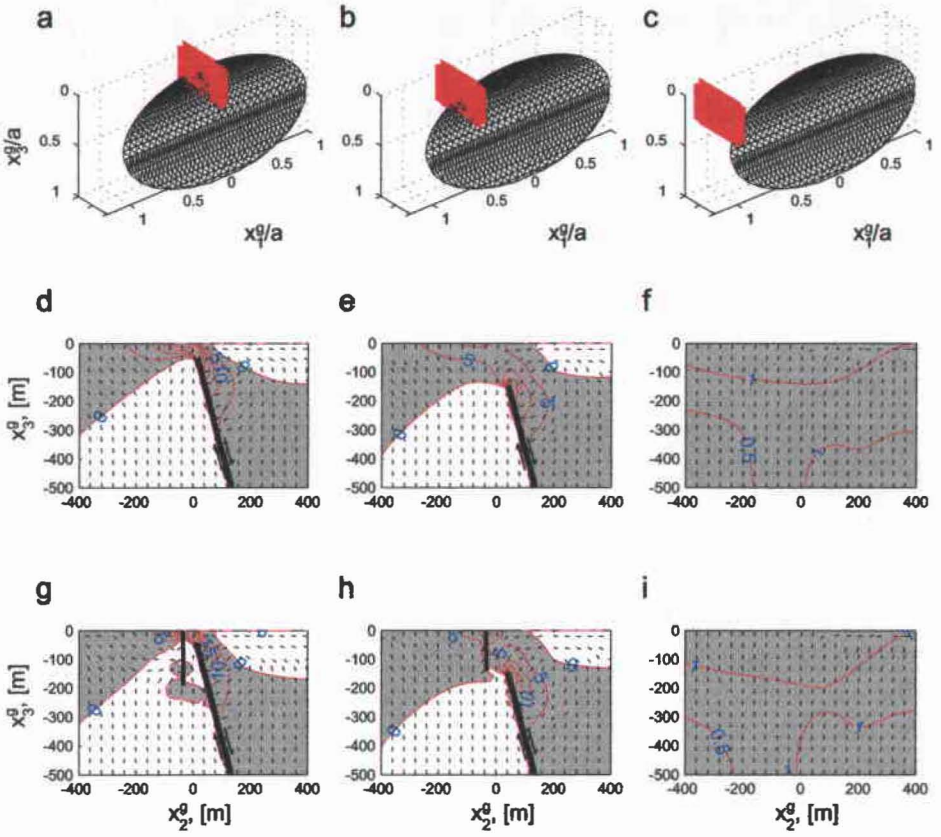

Figure 19: Stress fields in vertical planes. The top row shows the locations of the observation planes. The middle row shows σ_1 and trajectories perpendicular to σ_1 near an isolated fault with its upper tip at 50m depth. The bottom row shows σ_1 and trajectories perpendicular to σ_1 near a fault with its upper tip at 50m depth and a fissure with maximum depth of 200m. Gray regions indicate where σ_1 is tensile.

of the belt of opening mode fractures on the hangingwall of the Hopena fault. The tensile stress concentration is further away from the scarp than the compressive stress concentration of Fig. 18i. At the end of the Hopena fault scarp this belt terminates at an acute angle to the scarp. The model results suggest that the belt of fractures on the hangingwall forms when the upper tip of the blind fault is at shallow depth.

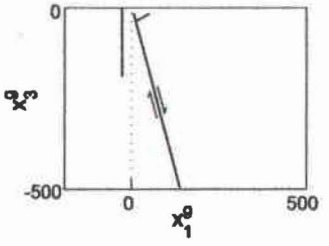

Figure 20: Along strike view of fault, fissure, and antithetic structure.

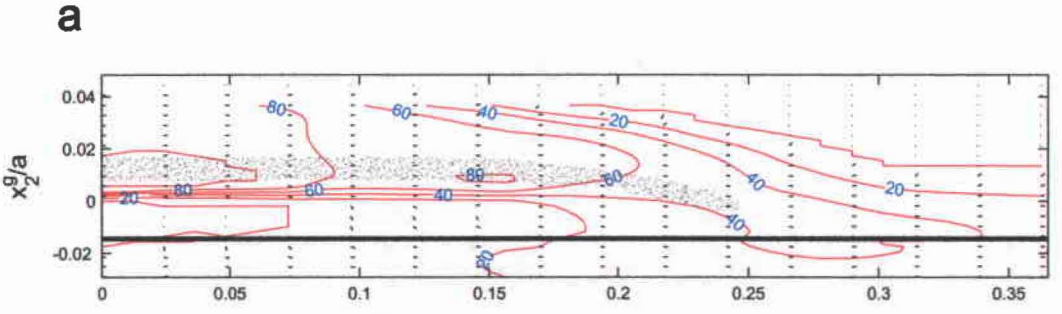

Figure 21: Stress field near a fault, a fissure, and an antithetic fracture. The upper tip of the fault is at 15m depth, a vertical fissure extends to a depth of 200m (black line), and an antithetic fracture at the upper fault tipline below the surface is roughly normal to the fault plane. Magnitudes of σ_1 and trajectories normal to σ_1 are depicted. The stippled region indicates a region that may correspond to the belt of fractures on the hangingwall.

4 Discussion

The focus of this study is to understand the growth of a surface-breaching fault. To address this, the field observations and analyses concentrated on how a growing fault would displace and fracture the surrounding rock. Surface-breaching faults could grow down from the surface or up from depth. Three-dimensional elastic models for the former scenario yield results inconsistent with the field observations. Three-dimensional elastic models of a fault growing up from depth do account the observed deformation in the field.

The general pattern of structures along the northern fork of the Hopena fault is characteristic of many Koae faults. The pattern consists of a breached monocline at the surface, three belts of fractures, and buckles near the base of the scarps. The analyses show that slip on a blind normal fault generates a monoclinal flexure of the ground surface. Field observations show that the monoclinal flexure is preserved after the fault breaches the surface. Fissures on the footwall are consistent with the tensile stress concentration above an isolated blind fault. Trajectories of principal stresses indicate that opening-mode fractures should strike parallel or sub-parallel to the fault trace on the footwall. The echelon pattern of fractures along and past the Hopena fault scarp is accounted for by tensile stresses above and past the model fault trace. Trajectories of tensile stress concentrations along the position of the scarp above a blind fault in the model match the strike of fractures in the field. High compressive stress concentrations prevail near the scarp on the hangingwall. Model stress trajectories at the base of the scarp indicate a fault-parallel trend of buckles, consistent with the field observations.

The models also indicate that fractures along the scarp that open in response to slip on a buried fault will tend to slip left-laterally as the fault grows (Fig. 22). This is consistent with the field observations. Subsurface stress fields indicate that fissures on the footwall of a normal fault may open up to approximately the depth of the upper tip of the fault itself. Opening along those fissures can be substantial in

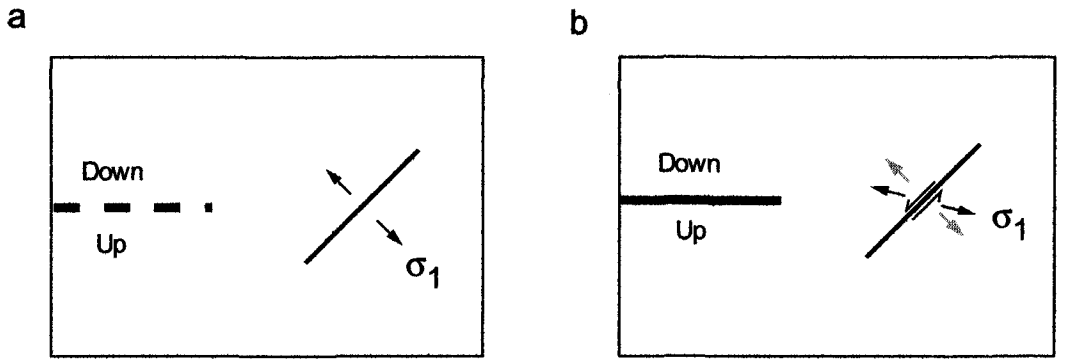

Figure 22: Stress rotation near the trace end. (a) Opening mode fractures may form at the surface for a blind fault. Arrows indicate the orientation of most tensile stress. The thick, dashed line depicts the projected fault-surface intersection. (b) Once the fault breaches the surface, principal stresses rotate (black arrows, gray arrows depict previous stress direction). Relative displacements on the pre-existing fracture are strike-slip (thin barbed arrows). The thick line indicates the fault trace.

the field as well as in numerical analyses of traction-free fissure on the footwall. The tendency for fissures to remain open changes when the fault breaches the surface. In a model with a traction-free fissure on the footwall, the fissure walls interpenetrate. This is both physically impossible and inconsistent with the field observations of gaping fissures. The propping effect of debris from the fissure walls may explain the persistence of gaping fissures on the footwall near a normal fault that has breached the surface. Fissures that are wedged open exert little qualitative effect on the stress solutions at the surface of an isolated fault.

Once a normal fault breaches the surface, the stress concentrations shift towards the ends of the fault scarp trace, with fault-normal tension prevailing on the footwall and fault-normal compression on the hangingwall. Echelon fractures along and past the scarp can also be accounted for with the fault and fissure model. The pattern of relative displacements across previously opened fractures near the fault scarp and the fissure is of the same left-lateral sense as it is for isolated faults that breach the surface.

The inclusion of an antithetic fracture at the upper tipline of the fault in the model runs can explain the hangingwall fractures. Antithetic fractures might develop over a range of depths. Their presence near the surface in the model induces tension on the hangingwall at the approximate location of hangingwall fractures. Once a model fault breaches the surface, the tensile stress field along the entire upper part of the fault plane diminishes. This would inhibit new antithetic fractures from forming and thus impedes the opening of more fractures at the surface on the hangingwall. These results may explain the termination of hangingwall fractures at the eastern end of the fault scarp.

The field observations and model results together support a growth process that can be outlined as follows (Fig. 23):

(1) Faults initiate at depth and propagate to the surface. Antithetic fractures may nucleate at all depths near the propagating fault tipline.

(2) Fractures on the footwall open up as the surface is flexed.

(3) Echelon fractures open right at the future scarp.

(4) Fractures on the footwall grow larger, evolving into fissures. Debris breaks off the fissure walls and accumulates in the opened fissure.

(5) As a fault propagates closer to the surface, non-elastic deformation including accumulation of the debris in the gaping fissures serves as a wedge, keeping the fissure from closing.

(6) Buckles develop near the base of the future scarp.

(7) Antithetic fractures in the subsurface cause fractures to open at the surface on the hangingwall.

(8) Once the fault breaches the surface, new buckles form only near the end of the fault scarp. New echelon fractures form past the end of the fault scarp. Preexisting echelon fractures experience a rotation in stresses as the tipline propagates up and laterally, causing strike-slip on these fractures near the scarp end. Fractures on the hangingwall terminate at the ends of fault scarps as tensile stress concentrations

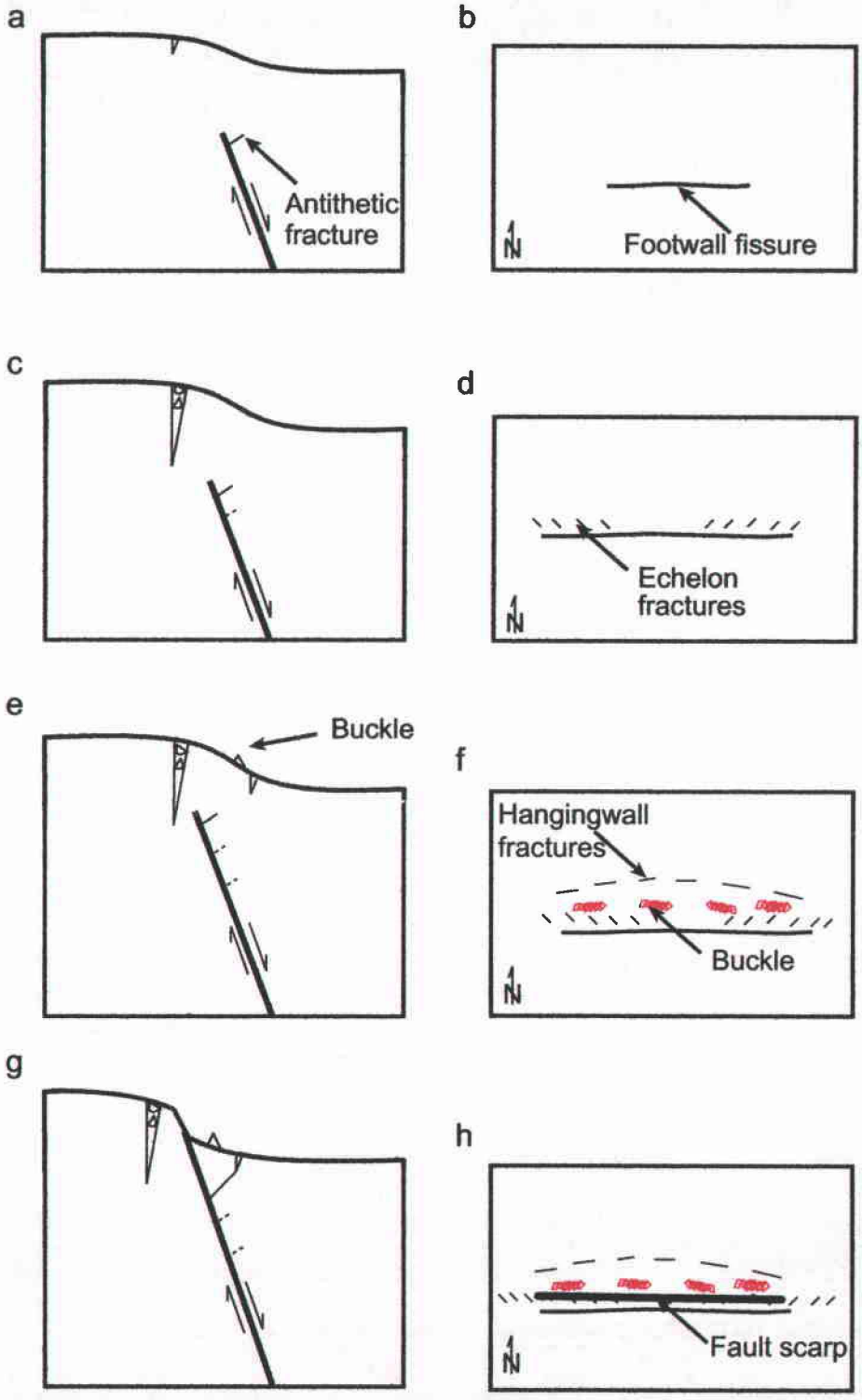

Figure 23: Growth history cartoon. Rows depict successive stages in the growth history. The left column shows along strike cross-sections. The right column depicts map views.

vanish along the entire fault plane near the upper tipline and antithetic fractures are thus kept from forming.

The scenarios presented here explain the origin and order in which deformation occurs at the surface. This order resembles the one by Duffield (1975) for the Koae faults in general. The general pattern of the structures near the northern fork of the Hopena fault also appears to resemble the pattern along faults in Iceland (Grant and Kattenhorn, 2004). The consistent pattern of fractures along the faults suggests that the evolution of normal faults as described here may be a common process.

5 Conclusions

The Hopena fault displays a systematic pattern of deformation at the surface:

(1) A breached monoclinal along the scarp;

(2) A belt of pronounced, steep fractures on the footwall;

(3) A belt of echelon fractures along the fault scarp and past its end;

(4) Buckles at the base of the scarp;

(5) A belt of fractures on the hangingwall;

(6) Left-lateral strike-slip on echelon fractures east of the scarp.

Elliptical normal faults growing up from depth can account for these features, but normal faults growing from the surface cannot. The latter does not provide an explanation for monoclinal warping across the fault trace, footwall fractures and fissures, hangingwall fractures, or buckles at the base of the fault scarp.

The three-dimensional analyses here expand the previous two-dimensional analyses by Langley (2001) by accounting for echelon fractures, hangingwall fractures, and the left-lateral strike-slip on echelon fractures past the fault trace end. The tipline shape, the three-dimensional kinematics and the effects of along strike propagation, which two-dimensional analyses cannot address, provide a more complete understanding of the growth of a normal fault.

The general pattern of deformation that occurs on the Big Island of Hawai'i resemble that in Iceland. This suggests that many normal faults may grow from depth rather than from the surface down.

Part II

Evolution of Normal Fault Tiplines

Abstract

Normal faults growing in the Earth's crust are subject to effects of the ground surface and secondary fractures that form in response to slip on the fault. Three-dimensional boundary element numerical models are used to evaluate the propagation tendencies of planar faults of elliptical tipline shape. Previous analyses of shallow, isolated fault below the ground surface indicate that the fault would tend to grow preferentially up-dip, thus attaining a tall rather than long shape. However, such shapes of faults are rarely observed in nature. Analyses that include secondary fractures that develop due to slip on the fault indicate that the fractures impede the tendency to grow up-dip. Antithetic fractures forming along the upper tipline of the fault have a particularly substantial influence on up-dip propagation.

1 Introduction

Normal faults in nature tend to be several times longer than they are tall (Rippon, 1985). Qualitative and kinematic explanations for commonly observed fault shapes can be found in the literature (e.g. Nicol et al., 1996; Walsh and Watterson, 1988), but only a few studies have addressed the propagation tendencies of normal faults in light of mechanical principles (Lin and Parmentier, 1988; Rudnicki and Wu, 1995; Kattenhorn and Pollard, 1999; Crider and Pollard, 1998). Lin and Parmentier (1988) investigated quasi-static fault propagation under the influence of lithostatic and tectonic loading, with slip controlled by frictional sliding laws (Byerlee, 1978). Their modeling results reveal that under constant tectonic loading the upper tip should propagate more readily than at the lower tip. Their two-dimensional analysis, however, did not consider three-dimensional aspects of fault growth or field observations that bear on the mechanics of fault propagation. Rudnicki and Wu (1995) considered depth-dependent loading and Mohr-Coulomb frictional slip criteria in two dimensions. They found that the ground surface promoted the up-dip propagation of shallow normal faults for a broad range of loading conditions. They did not, however, investigate possible effects that restrict upward fault growth or account for field observations of fault structures that might bear on normal fault growth. Kattenhorn and Pollard (1999) extended the previous studies to three dimensions and investigated the effects of lithostatic loading on three-dimensional normal faults subject to friction. They concluded that lithologic heterogeneity can influence where normal faults nucleate, impede their upward growth, and lead to normal faults being longer than tall. The possible effects of other factors on fault shape have been explored little.

The controls on fault geometry are important, for fault geometry exerts a fundamental control on fault behavior (Segall and Pollard, 1983). This study investigates the mechanics of normal fault growth, with a specific focus on the effect of secondary fractures generated by slip. Secondary fractures affect fault processes in a variety of

ways. Secondary fractures not only form in response to faulting but also strongly influence subsequent fault growth (Segall and Pollard, 1983; Bürgmann et al., 1994; Bruhn, 1994; Antonelli and Aydin, 1995). They contribute to the mechanical linkage of previously discontinuous faults (Segall and Pollard, 1983; Martel and Boger, 1998) as well as the hydraulic linkage between segmented faults (Gudmundsson, 2000; National Academy of Sciences, 1996). Since conditions near the fault tipline play important roles in the initiation and termination of earthquake ruptures, secondary fractures there potentially allow insight into slip behavior of the fault and may form as precursors to co-seismic slip (King and Nábêlek, 1985).

The effects of structures observed in the field and inferred to exist from mechanical analyses during the growth of a normal fault are investigated here. Part I of this thesis described the evolution of one fault, the Hopena Fault of the Koae Fault System on the Big Island of Hawai'i, using mechanical models guided by detailed field observations. One key conclusion is that secondary structures at the surface and below are an intricate part of fault growth. Here, I examine the evolution of an isolated fault and specifically take into account the possible effect of secondary structures on fault growth. The interplay of numerical modeling and use of detailed field observations complement each other and shed light on the growth of normal faults.

2 Field Data and Kinematics

The normal fault investigated in detail here, the Hopena fault, is part of the Koae fault system (KFS). Structures along the Hopena fault are abundant and diverse, but they form a systematic pattern. Significantly, the pattern along the Hopena fault is encountered along many other faults in the KFS as well. The systematic pattern includes three belts of fractures. One is located on the footwall of the fault, the second is along the fault scarp, and the third is on the hangingwall. The footwall fractures strike ENE, essentially parallel to the fault strike, are approximately vertical, and extend along the entire length of the Hopena fault scarp. One of the footwall fractures has an aperture of $\sim$ 140cm and is termed a fissure in the subsequent discussion. Footwall fissures are common to most faults in the KFS. They are usually located within a few tens of meters of the fault scarp, about 25m in the case of the Hopena fault. Past the fault trace end, these fractures curve to the north. The fractures along the scarp extend past the trace end and retain a right-stepping echelon pattern. The hangingwall fractures are sub-parallel to the fault and individual fractures open much less than those on the footwall. The belt of hangingwall fractures essentially terminates at the end of the fault scarp. Hangingwall fractures are observed along many faults in the KFS.

Part I discusses the formation and kinematics of the secondary fractures, focusing on those in the footwall and hangingwall. I concluded that the systematic patterns are formed during different stages of growth of the Hopena fault in a manner generally consistent with the description of Duffield (1975). The fissures appear to form due to a tensile stress concentrations and flexure of the ground surface when the fault is blind. Once the fault breaches the surface, mechanical modeling results suggest that the fissures should tend to close, but this is inconsistent with field observations (see part I and Langley, 2001). Blocks that broke off the fissure walls typically obstruct the fissures. The field observations and previous modeling suggest that the fissures are kept from closing by non-elastic deformation, such as the propping action

of the blocks.

A further conclusion of part I is that the fractures that open on the hangingwall are induced by subsurface deformation in the form of antithetic fractures. The effect of the antithetic fractures, however, is only felt at the surface when the upper tipline of the fault is at very shallow depths. Fracturing on the footwall surface most likely precedes opening of fractures on the hangingwall surface. The described pattern of deformation on the surface is characteristic of normal faults in the KFS.

3 Mechanical Analysis of Tipline Evolution

The goal is now to investigate the effects of the typical secondary features (i.e. footwall fissures and antithetic hangingwall fractures) on the fault shape itself using fracture mechanics principles. The initial analyses are for a single fault at depth. Subsequent analyses account explicitly for the presence of a fissure on the footwall and an antithetic fracture near the upper tipline on the hangingwall. As will be shown, the analyses indicate that fractures resulting from faulting are likely to alter how the fault grows.

3.1 Model Fault Geometry

Three-dimensional data indicate that many normal faults in nature tend to have a roughly elliptical tipline shape (Rippon, 1985). Faults here are idealized by ellipses (Figs. 24). Common aspect ratios of elliptical faults range from $\frac{b}{a} = \frac{1}{8}$ to $\frac{2}{1}$, where b is the down-dip semi axis length and a is the along strike semi axis length. (Nicol et al., 1996). The analyses here consider planar faults that have a constant aspect ratio of $\frac{b}{a} = \frac{1}{2}$. All faults dip at 75° as results of fault parameter inversions using topographic data favor this dip over dips of 65° or 85°.

Guided by the field observations, the results from the isolated model fault in part I, and the results of Langley (2001), a vertical fissure is included in the model runs. The fissure aperture is prescribed and the walls are free of any shear tractions. The opening prescribed on the model fissure is consistent with $\sim$ 1.4m maximum aperture of the fissure at the surface near the Hopena fault. The fissure is represented by the lower half of an ellipse centered at x_2^g = -25m (see part II section 3.4 for coordinate axes systems). The fissure is 2.5km long and extends from the surface vertically to a depth of 200m.

Models of blind faults and of blind faults with a footwall fissure predict large tensile stress concentrations, and hence fracturing, near the upper tipline of the fault

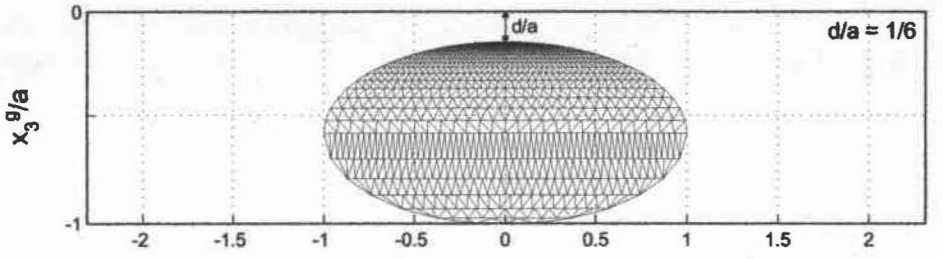

Figure 24: Single model fault

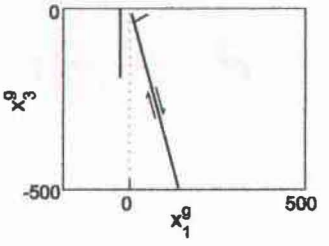

Figure 25: View of fault, fissure, and antithetic structure along strike.

on the hangingwall (see part I). The trajectories of principal stresses indicate that orientations of secondary fractures at the upper tipline on the hangingwall would strike parallel to the fault and be roughly perpendicular to the fault plane (see part I). This pattern is reproduced for faults at many depths. To simulate this fracturing, an antithetic fracture is included as a traction-free half-ellipse extending over $\sim$ 80% of the length of the fault near the upper tipline. The upper tip of the antithetic fracture is at roughly the same depth as the upper tip of the fault is (Fig. 25). This single model fracture represents what could be a series of fractures along a real fault. To simulate elliptical faults growing toward the surface, their size is increased, but their aspect ratio is retained.

3.2 Propagation Tendencies

The analyses of the Hopena fault and the key features near it may provide an explanation for some controls of fault shape. The evolution of a fault depends on the

change in tipline geometry of the fault, which in turn is governed by the stress state prevalent close to the tipline (Rice, 1968; Rudnicki, 1980). The near-tip stresses can be written in the following form (Lawn and Wilshaw, 1975):

$$\sigma_{ij}(r,\theta) = \frac{K_m}{\sqrt{2\pi r}} f_{ij}(\theta) \tag{1}$$

Near-tip displacements, measured relative to the fracture tip, are of the following form:

$$u_i(r,\theta) = K_m \sqrt{r} h_i(\theta) \tag{2}$$

In the above equations, r is the distance from the tipline, the functions f and h account the angular position around the perimeter out of the fault plane, and K_m are stress intensity factors. Three stress intensity factors exist. They account for opening of fractures (K_I), sliding perpendicular to the tipline (K_{II}), and tearing parallel to the tipline (K_{III}), (Fig. 26). In an isotropic, elastic medium the stress intensity factors thus can be related to near-tip displacement discontinuity across the fracture, $\Delta u_i = u_i(r,+\pi) - u_i(r,-\pi)$. The displacement discontinuities for modes II and III are:

$$\Delta u_{II}(r) = \frac{-K_{II}}{\mu}\sqrt{\frac{r}{2\pi}} 4(1-\nu) \tag{3}$$

$$\Delta u_{III}(r) = \frac{K_{III}}{\mu}\sqrt{\frac{r}{2\pi}}. \tag{4}$$

Propagation tendencies of fractures may be described using the fracture energy release rate, $\mathcal{G}$ (Kattenhorn and Pollard, 1999; Willemse and Pollard, 2000; Martel, 2004). The quantity $\mathcal{G}$ is a measure of strain energy loss rate associated with the incremental growth of the fault surface area. It can be calculated in terms of the stress intensity factors (Lawn and Wilshaw, 1975). For shear fractures, $K_I = 0$ and $\mathcal{G}$ is of the following form for in-plane shear fracture propagation (Lawn and Wilshaw, 1975):

$$\mathcal{G} = \frac{(1-\nu)}{2\mu}\left\{K_{II}^2 + \frac{K_{III}^2}{(1-\nu)}\right\} \tag{5}$$

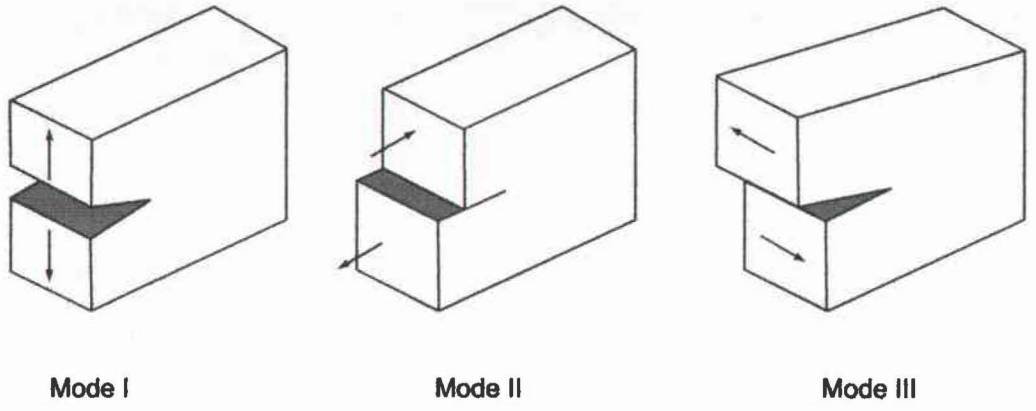

Figure 26: Fracture modes of fractures and faults. Mode I refers to opening of fractures, Mode II refers to tipline - normal sliding, Mode III refers to tipline parallel tearing.

where μ is the shear modulus. By substituting equations (3) and (4) into (5), $\mathcal{G}$ can be rewritten as:

$$\mathcal{G} = \frac{(1-\nu)}{2\mu}K_{II}^2 + \frac{1}{2\mu}K_{III}^2 = \frac{\pi\mu}{r}\left\{\frac{1}{16(1-\nu)}\Delta u_{II}^2 + \Delta u_{III}^2\right\} \qquad (6)$$

The relationships above are adapted for use with Poly3D by replacing the distance r by the shortest distance from the element midpoint to the perimeter, d, and multiplying the right side by a constant (C). The constant accounts for the stair-stepping approximation of a smooth slip distribution on the fault plane. The expressions resemble those of equations (3) and (4),

$$K_{II} = \frac{-C\mu D_{II}}{4(1-\nu)}\sqrt{\frac{2\pi}{d}} \qquad (7)$$

$$K_{III} = C\mu D_{III}\sqrt{\frac{2\pi}{d}} \qquad (8)$$

where D_i are the mode II and III slip components at the centroids of tipline elements.

Analytical solutions for stress intensity factors exist for simple fracture geometries (e.g. ellipses), and simple loading conditions, (Kassir and Sih, 1966; Tada et al., 2000); see also appendix 1. Stress intensity factors for fractures with complicated geometries and loading conditions must be evaluated numerically. In this study, the

fault geometries are idealized as elliptical, for which analytical solutions in a full-space exist for uniform driving stress. The driving stress is the shear strength loss on the fault during slip. The ratio of the exact half-space solution (${\mathcal{G}_{hs}}^{exact}$) to full-space solution (${\mathcal{G}_{fs}}^{exact}$) is well approximated by the ratio of the numerical half-space solution (${\mathcal{G}_{hs}}^{num}$) to numerical full-space solution (${\mathcal{G}_{fs}}^{num}$). Therefore, the energy release rate in a half-space is determined as follows (Martel, 2004):

$$ {\mathcal{G}_{hs}}^{exact} \approx {\mathcal{G}_{fs}}^{exact} \frac{{\mathcal{G}_{hs}}^{num}}{{\mathcal{G}_{fs}}^{num}} \tag{9} $$

Calculations for $\mathcal{G}$ allow inferences of propagation tendencies along the tiplines of idealized, elliptical faults (Kattenhorn and Pollard, 1999; Willemse and Pollard, 2000; Martel, 2004). Locations where $\mathcal{G}$ is largest around the tipline of faults are likely locations of fault growth, although no critical energy release rate is explicitly assigned here. The analyses of $\mathcal{G}$ shed light on the propagation of normal faults in the vicinity of the free surface and under the influence of secondary structures.

3.3 Ambient Stress Field and Fault

A realistic representation of the regional stress conditions is needed to reflect the geologic setting on the south flank of Kilauea. The ambient stresses are complicated, being influenced by the presence of Mauna Loa, the rift zones and the relatively unconfined southern flank of Kilauea. Mauna Loa serves as an abutment to the north. The ambient stresses probably vary in time also as dikes intrude along the rift zones and earthquakes occur (Rubin and Pollard, 1987; Lipman et al., 1985). I follow the suggestions of Swanson et al. (1976) and consider the south flank to be close to laterally unconstrained. Here, for simplicity, the horizontal stresses normal to the fault strike are considered to be zero. A constant compressive (negative) stress is assigned parallel to the fault strike, and the vertical normal stresses due to gravity vary linearly with depth. This representation of the ambient field is consistent with the orientation of the Koae faults and their sense of slip (Swanson et al., 1976). This

is an idealization of a stress field that is acknowledged to be complicated.

The assignment of the ambient stress field and the resolution of tractions on boundary elements makes use of several coordinate axes systems (CAS). The notation x_i^g refers to the global reference system with x_1^g parallel to fault strike, x_2^g horizontal and perpendicular to fault strike, and x_3^g up (Fig. 27). Two local reference frames are used as well. One, x_i^e, used for to tractions acting at the centers of the polygonal elements, has x_1^e pointing down-dip, x_2^e pointing along the strike of the element, and x_3^e pointing normal to the element plane and up (Fig. 27). The second local reference frame, $x_i^{e'}$, is defined with $x_3^{e'}$ in the fault plane and parallel to the tipline, $x_2^{e'}$ in the fault plane and normal to the tipline , and $x_1^{e'}$ normal to the fault plane (Fig. 27). This second reference frame is used to evaluate mode II and mode III displacements.

A representation of the total stress field (Fig. 28) is achieved by superposing the perturbation associated with fault slip and the ambient stress field (Martel and Muller, 2000). The ambient stress field is represented by a vertical compressive stress that increases linearly in the $-x_3^g$ direction and a constant compressive stress assigned parallel to the fault strike:

$$\sigma_{33}^g = \rho\, g\, x_3^g \tag{10}$$

$$\sigma_{22}^g = -1MPa \tag{11}$$

$$\sigma_{11}^g = 0. \tag{12}$$

All other components of σ_{ij}^g are equal to zero. In the above equations g is the gravitational acceleration, ρ is rock density, ν is Poisson's ratio. Values of the material parameters are $\rho = 2700\ kg \cdot m^{-3}$, $\nu = \frac{1}{4}$, and E (Young's modulus) = 5000MPa (Langley, 2001).

All fault elements are kept from opening or interpenetrating by prescribing a Burger's vector component, b_3^e of zero at each element center. A complete shear stress drop is assumed on the entire fault plane. This maximizes slip and yields the maximum stress perturbation in the surrounding rock. The result here thus serves as

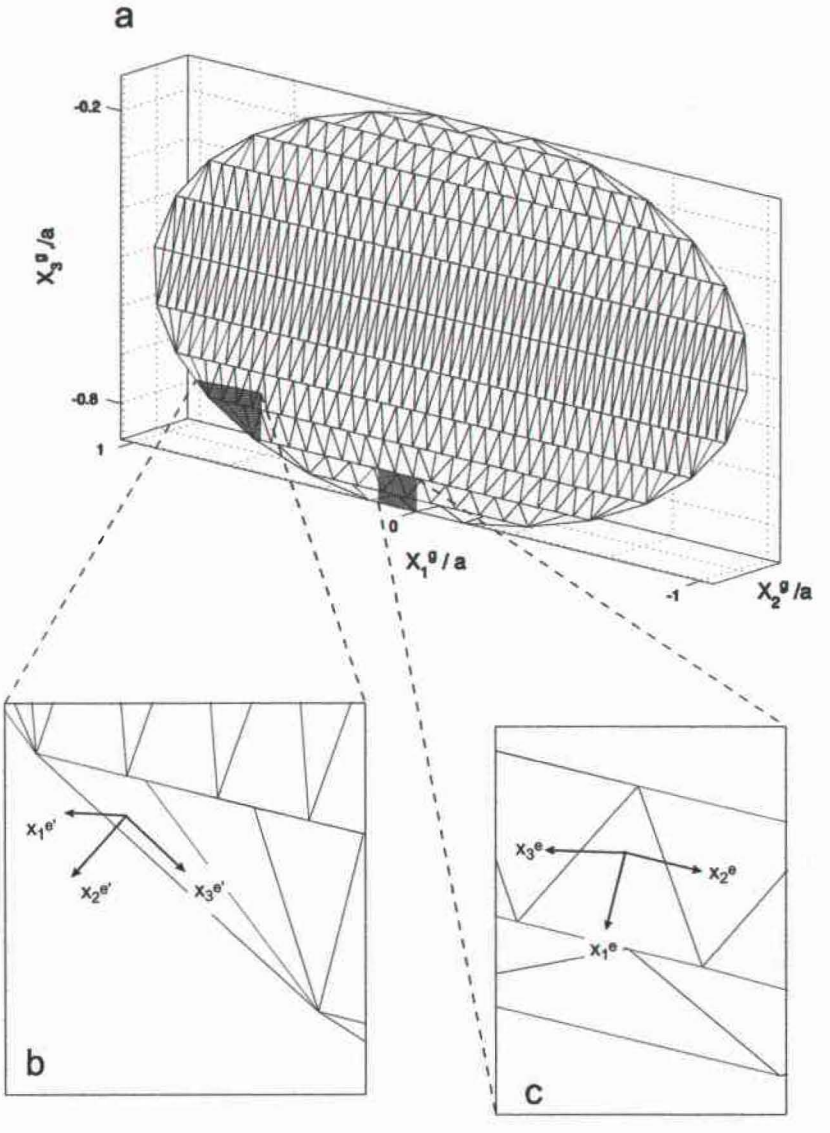

Figure 27: Discretized elliptical fault with (a) global CAS, and (b, c) local element CAS. x_1^e points down dip, x_2^e points along the strike of the fault, x_3^e is normal to the fault plane and up.

an end member. To account for the effects of gravity and achieve a complete shear stress drop on the fault plane, the negative of the resolved gravity-induced traction, t_1^e, is prescribed at the center of each element comprising the fault plane. The tractions on the fault elements are calculated using Cauchy's formula (Lai et al., 1993):

$$b_3^e = 0 \tag{13}$$

$$t_1^e = \rho\, g\, x_3^g\, cos(\delta)\, sin(\delta) \tag{14}$$

$$t_2^e = 0, \tag{15}$$

where δ is the dip of the fault (75°). The boundary conditions in equations (13)-(15) are associated with the perturbation due to fault slip and reflect the central box depicted in figure 28. Superposed on the perturbation is the ambient stress field (equations (10)-(12)).

3.4 Boundary Element Method

In this analysis, fracture mechanics principles are employed. They were first introduced by Griffith (1921) and have been applied to a variety of rock fracture phenomena (e.g. Pollard and Aydin, 1987), including normal faulting (e.g. Willemse and Pollard, 2000).

The analyses here are carried out with Poly3D, a three-dimensional boundary element method (BEM) numerical code (Thomas, 1993). In this method the fault or fracture surface is divided into contiguous polygonal elements, each of which accommodates a constant amount of relative displacement. The displacement discontinuities across all elements are found by solving a system of linear equations that describes the influence of the elements on one another and that simultaneously satisfies the given boundary conditions. The separate boundary element solutions satisfy the governing partial differential equations for linear elasticity in a half-space. The domain requires no discretization and the number of linear equations solved is smaller than for other numerical techniques for solving partial differential equations such as finite element

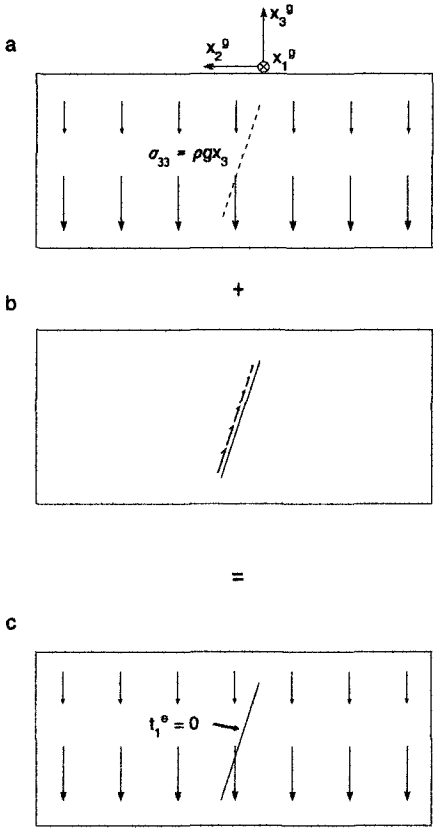

Figure 28: Cartoon showing how the stresses are solved for. (a) The ambient stress field. (b) Perturbation due to fault slip. (c) The superposition of (a) and (b) yields the total stress field with a shear traction-free fault.

methods (Crouch and Starfield, 1983). Poly3D allows two types of boundary conditions to be specified at the center of each element. Either Burger's vector components or tractions can be specified. This study uses a right-handed coordinate axes system and tension is positive. The code calculates displacements and the local stress tensor at points on a defined observation grid. A limitation of this routine is that Poly3D calculates the stress and displacement field for a single slip event, but cannot include the effects of previous slip events on the surrounding material. Tests on simple fault shapes for which analytical solutions exist show that Poly3d reproduces analytical results to within a few percent (Crider and Pollard, 1998).

3.5 Results

The focus here is on the effect of secondary features on the propagation tendencies of a fault at depth. The two nearby structures are a surface fissure on the footwall of the fault and an antithetic fracture near the upper tipline on the hangingwall of the fault. The effects of each structure are addressed separately to isolate them.

The energy release rate for an isolated elliptical fault, $\mathcal{G}^{iso}$, is plotted against angular position along the upper tipline in Figure 29. Faults at depths of 400m and 250m, show almost constant values of $\mathcal{G}$. Faults with upper tips at depths of 100m to 50m exhibit local maxima of $\mathcal{G}$ near the upper tip and the lateral tips of the fault. These local maxima become more pronounced for shallower tiplines, with the value of $\mathcal{G}$ increasing the most for the crest of the tipline.

I assume that positions where $\mathcal{G}$ is high are favored locations for fault growth (e.g. Martel, 2004). The $\mathcal{G}$ values are consistent with the interpretation that faults at depth would essentially maintain their shape as they grow. Shallow faults would tend to become tall rather than long for the geometry and loading conditions of this model. The increased propagation tendency along the top of the tipline reflects in part the influence of the ground surface as well as greater slip on the fault as it increases in size at shallower depth. The results for isolated faults are consistent with the three-dimensional analyses of isolated frictional faults subject to lithostatic loading Kattenhorn and Pollard (1999).

The normalized energy release rate, $\frac{\mathcal{G}^{fiss}}{\mathcal{G}^{iso}}$, is plotted against angular position along the upper tipline of an elliptical fault with a nearby fissure that extends to a depth of 200m in Figure 30, where $\mathcal{G}^{fiss}$ is the value for $\mathcal{G}$ with the fissure present. For faults with the upper tips at 200m and 400m depths, plots of $\frac{\mathcal{G}^{fiss}}{\mathcal{G}^{iso}}$ indicate that the fissure has little, if any, influence on the propagation tendencies of the fault. However, when the upper tip is at 100m depth, and the fissure vertically overlaps the fault, the value of $\frac{\mathcal{G}^{fiss}}{\mathcal{G}^{iso}}$ at the top of the tipline drops compared to the case where the fissure

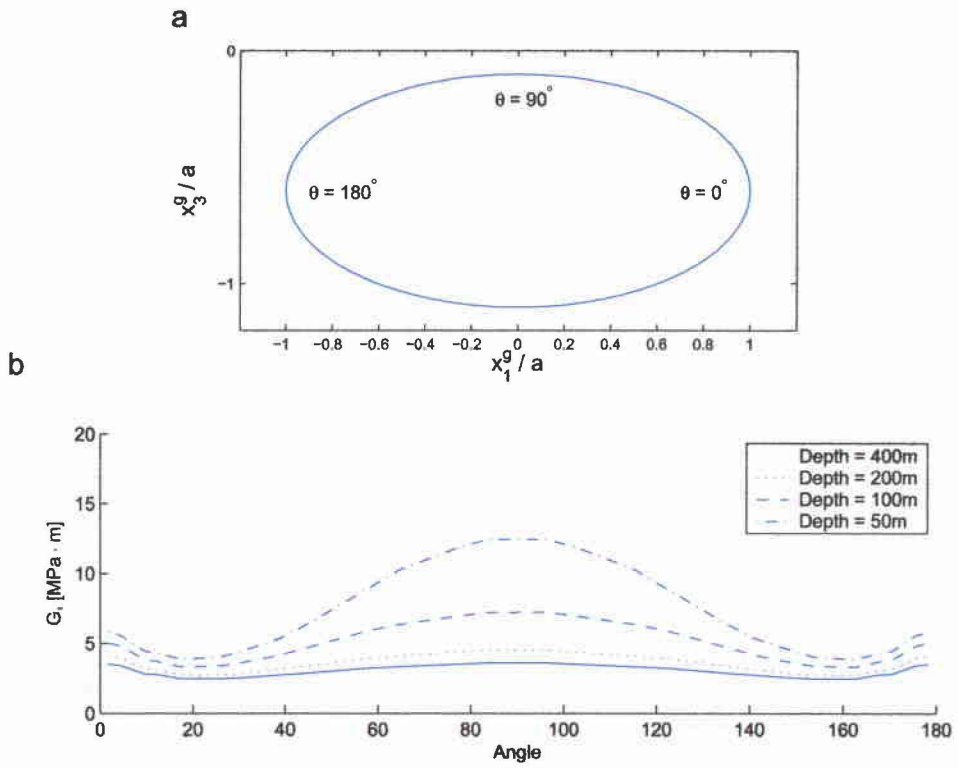

Figure 29: (a) Angular position along the upper half of elliptical faults. (b) Energy release rate, $\mathcal{G}^{iso}$, for isolated faults at different depths. Angles correspond to locations at the perimeter of the fault.

is absent (Fig. 29). A secondary structure near a blind fault thus can influence the shape and evolution of the fault.

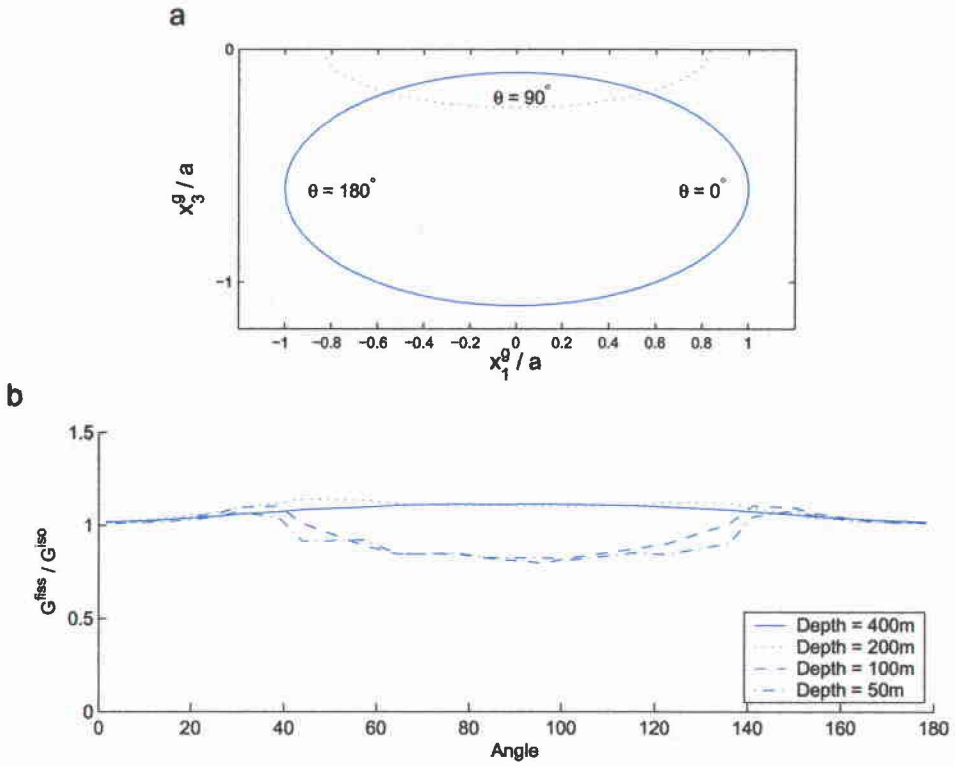

Figure 30: (a) Angular position along the upper half of an elliptical fault, e.g. upper tip at 100m, and nearby fissure. (b) Energy release rate, $\mathcal{G}^{fiss}$, normalized by $\mathcal{G}^{iso}$ for faults at different depths influenced by a nearby fissure.

I now turn to the case of a fault with an antithetic fracture near its upper tip (Fig. 31). The fissure is not present here. Antithetic fractures or joints commonly form at high angles to faults (e.g. Kattenhorn et al., 2000). The angle to the fault plane has an effect on $\mathcal{G}$, but for brevity $\mathcal{G}$ is only evaluated for one angle, 80°. The normalized value of $\frac{\mathcal{G}^{anti}}{\mathcal{G}^{iso}}$ is reduced sharply along portions of the tipline above the antithetic fracture, where $\mathcal{G}^{anti}$ is the value for $\mathcal{G}$ with the antithetic fracture present. Values of $\mathcal{G}$ are reduced by ~10% to ~ 90%, relative to the values where an antithetic fracture is absent, for a fault upper tip depth of 200m or less.

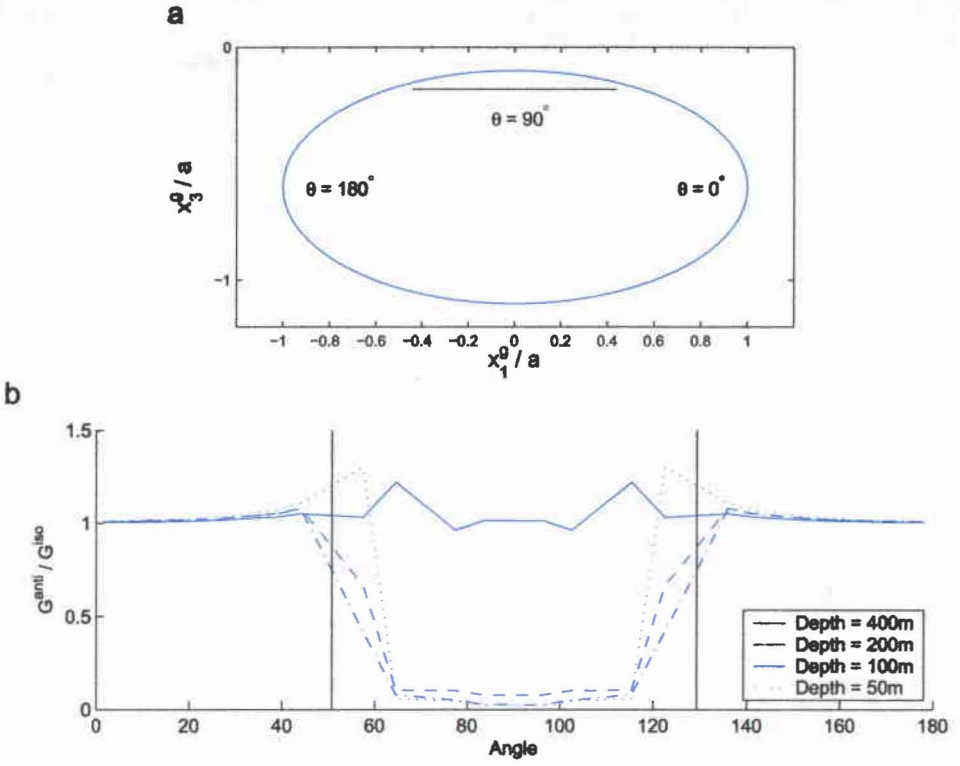

Figure 31: (a) Angular position along the upper half of elliptical faults with a nearby antithetic fracture. (b) Energy release rate, $\mathcal{G}^{anti}$, normalized by $\mathcal{G}^{iso}$ for faults at different depths influenced by a nearby antithetic fracture. The black line in (a) indicates the intersection between the fault and antithetic fracture. Black lines in (b) indicate the angles of overlap between the faults and the antithetic fractures.

This result strongly suggests that secondary fractures close to normal faults can substantially impede the up-dip growth of normal faults. It also suggests that normal faults might propagate laterally more readily than up-dip, possibly causing them to become much longer than they are tall.

4 Conclusions

Secondary features like footwall fissures and antithetic fractures are innate to the evolution of some normal faults. Mechanical modeling suggests that they form in response to fault slip, and that they also affect fault growth. Calculations for $\mathcal{G}$ for isolated normal faults predict that they would preferentially propagate up-dip and that normal faults would tend to be tall rather than long. A different story emerges if footwall fissures and antithetic fractures are accounted for. Nearby fissures on the footwall reduce $\mathcal{G}$ by roughly $\sim 25\%$ relative to isolated faults. The presence of antithetic fractures has fairly little effect when the fault is at deeper depths. The presence of the antithetic fracture reduces propagation tendencies of an isolated fault by $\sim 90\%$ when the fault tip is close to the surface. The reduction in $\mathcal{G}$ near the top of a fault could help explain why normal faults tend to be longer than they are tall.

A Appendix

A.1 Analytical Solution for $\mathcal{G}$ in a Full-Space

The following expressions were first introduces by Kassir and Sih (1966).

$$K_{II} = -\frac{\sigma \sin\gamma \cos\gamma \sqrt{\pi b} k^2}{\left\{ \sin^2\theta + \frac{b^2}{a^2}\cos^2\theta \right\}^{\frac{1}{4}}} \left\{ \frac{k'}{B}\cos\omega\cos\theta + \frac{1}{C}\sin\omega\sin\theta \right\} \quad \text{(A-1)}$$

$$K_{III} = \frac{\sigma \sin\gamma \cos\gamma \sqrt{\pi b}\,(1-\nu)\, k^2}{\left\{ \sin^2\theta + \frac{b^2}{a^2}\cos^2\theta \right\}^{\frac{1}{4}}} \left\{ \frac{1}{B}\cos\omega\sin\theta - \frac{k'}{C}\sin\omega\sin\theta \right\} \quad \text{(A-2)}$$

$$B = \left(k^2 - \nu\right) E(k) + \nu k'^2 K(k) \quad \text{(A-3)}$$

$$C = \left(k^2 + \nu k'^2\right) E(k) - \nu k'^2 K(k) \quad \text{(A-4)}$$

$$k^2 = 1 - k'^2 \quad \text{(A-5)}$$

$$k' = \frac{b}{a} \quad \text{(A-6)}$$

$$K(k) = \int_0^{\frac{\pi}{2}} \frac{d\varphi}{\sqrt{1 - k^2 \sin^2\varphi}} \quad \text{(A-7)}$$

$$E(k) = \int_0^{\frac{\pi}{2}} \sqrt{1 - k^2 \sin^2\varphi}\, d\varphi \quad \text{(A-8)}$$

See figure 32 for definitions of γ, ω, σ, θ, a and b. The driving stress, σ, is constant. Equations A-7 and A-8 contain elliptical integrals. Here, $\omega = 90$, and $\gamma = dip$, hence the following simplification apply.

$$K_{II} = -\frac{\sigma \sin\gamma \cos\gamma \sqrt{\pi b} k^2}{\left\{ \sin^2\theta + \frac{b^2}{a^2}\cos^2\theta \right\}^{\frac{1}{4}}} \left\{ \frac{1}{C}\sin\theta \right\} \quad \text{(A-9)}$$

$$K_{III} = \frac{\sigma \sin\gamma \cos\gamma \sqrt{\pi b}\,(1-\nu)\, k^2}{\left\{ \sin^2\theta + \frac{b^2}{a^2}\cos^2\theta \right\}^{\frac{1}{4}}} \left\{ -\frac{k'}{C}\sin\theta \right\} \quad \text{(A-10)}$$

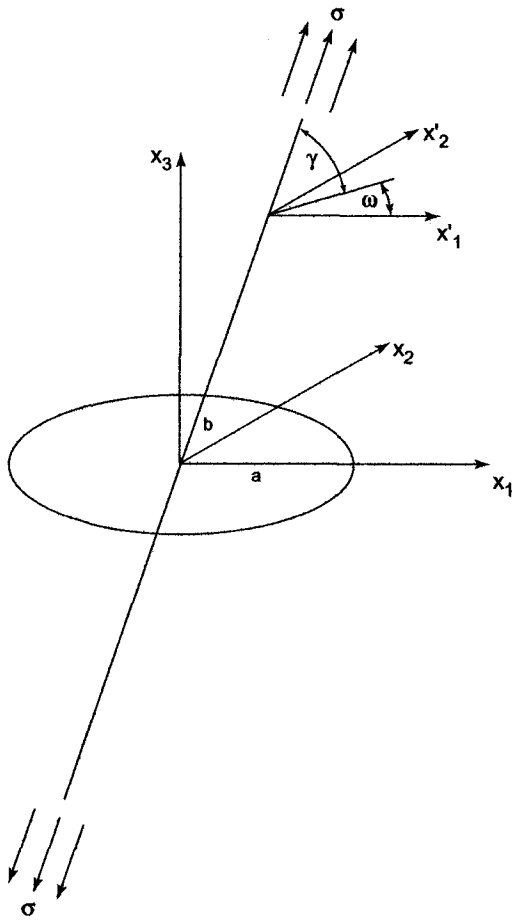

Figure 32: Figure showing the location of γ, ω, σ, θ, a and b.

A.2 Stress Orientations for Varied Boundary Conditions

A realistic representation of the regional stress conditions is needed to reflect the geologic setting. Ambient stresses in the KFS are influenced by the presence of Mauna Loa, the rift zones and the relatively unconfined southern flank of Kilauea. Mauna Loa serves as an abutment to the north. The south flank is being displaced to the south, and Swanson et al. (1976) have considered it to be close to laterally unrestricted. The dilation across the KFS is consistent with the relatively unrestricted seaward motion across the KFS (Delaney et al., 1993; Owen et al., 1995). The ambient stress field changes through time as dikes intrude along the rift zones and earthquakes occur at Kilauea (Rubin and Pollard, 1987; Lipman et al., 1985). The prevailing conditions thus remain somewhat enigmatic.

The emphasis of this study is the deformation near fault ends. Differences of principal stress orientations near the ends of elliptical faults due to varied ambient boundary conditions are evaluated here. Three different ambient conditions are considered here: (1) no ambient stresses, (2) fault-parallel compression without fault-normal compression, and (3) fault-parallel compression and fault-normal tension. Stress orientations for three geometries that idealize the successive stages of upward fault growth are investigated here.

Figure 33 depicts trajectories perpendicular to the most tensile stress for the three ambient stress scenarios near a blind fault (Fig. 33a) with its upper tip at $50m$ depth, a fault with its upper tip tangent to the ground surface (Fig. 33b), and a breached fault (Fig. 33c). For all geometries, the stress orientations on the footwall of the fault vary little. Along $x_2^g/a = 0$, stress orientations also vary little. On the hangingwall at some distance from the fault trace, stresses for condition (1) differ from conditions (2) and (3). The differences of principal stress orientation are most pronounced away from the ends of the faults. Near fault ends the differences are minimal. This is because the fault tip stress concentration dominates the contribution of the ambient field. For all sets of boundary conditions, stress orientations account

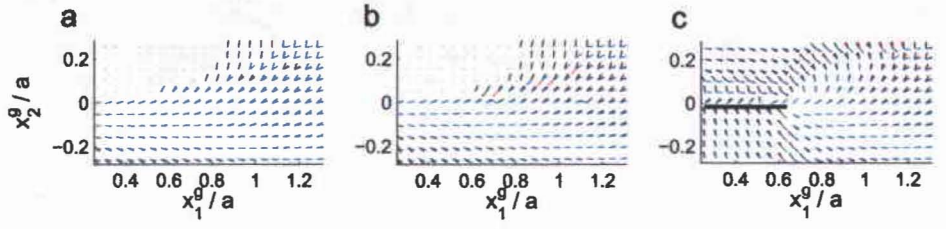

Figure 33: Trajectories perpendicular to the most tensile stress, σ_1 for varied ambient fields. Ambient stresses for black trajectories are: fault-parallel stresses = $(0MPa)$, fault-normal stresses = $(0MPa)$. Ambient stresses for red trajectories are: fault-parallel compressions $(2MPa)$, fault-normal stresses = $(0MPa)$. Ambient stresses for blue trajectories are: fault-parallel compression = $(2MPa)$, fault-normal compression = $(1MPa)$. (a) depicts the orientations of most tensile stresses above a blind fault with its upper tip at $50m$ depth. (b) depicts the orientations of most tensile stresses above a fault with its upper tipline tangential to the ground surface. (c) depicts the orientations of most tensile stresses near a breached fault.

for the general strike of fractures in all fracture belts near the Hopena fault. Although the prevailing ambient stresses remain elusive, principal stress orientations are not highly dependent on the ambient stress magnitudes.

References

Acocella, V., Korme, T. and Salvini, F. (2003) Formation of normal faults along the axial zone of the Ethiopian Rift. *Journal of Structural Geology*, **25**, 503-513

Ando, M. (1979) The Hawaii Earthquake of November 29,1975: Low dip angle faulting due to forceful injection of magma. *Journal of Geophysical Research*, **84**, 7616-7626.

Antonelli, M. and Aydin, A. (1995) Effect of faulting on fluid flow in porous sandstones: geometry and spatial distribution. *American Association of Petroleum Geologists Bulletin* **79**, 642-671

Barber, J.R. (1992) *Elasticity*, Kluwer Academic Publishers, Dordrecht

Bruhn, R.L. (1994) Fracturing in normal fault zones: Implications for fluid transport and fault stability, in, *The Mechanical Involvement of Fluids in Faulting, United States Geological Survey Open-File Report 94-228*, 1675-1690

Bürgmann, R, Pollard, D.D, and Martel, S.J. (1994) Slip distributions on faults: effects of stress gradients, inelastic deformation, heterogeneous host-rock stiffness, and fault interaction. *Journal of Structural Geology*, **16**, 1675-1688

Byerlee, J.(1978) Friction of rocks. *Pure and Applied Geophysics*, **116**, 615-626

Cartwright, J.A. and Mansfield, C.S. (1998) Lateral displacement and lateral tip geometry of normal faults in the Canyonlands National Park, Utah. *Journal of Structural Geology*, **20**, 3-19

Cervelli, P., Segall, P., Johnson, K., Lisowski, M. and Miklius, A. (2002) Sudden a-seismic fault slip on the south flank of Kilauea volcano. *Nature*, **415**, 1014-1018

Crider, J.G. and Pollard D.D. (1998) Fault linkage: Three-dimensional mechanical interaction between echelon normal faults. *Journal of Geophysical Research*, **103**, 24373-24391

Crouch. S.L. and Starfield, A.M. (1983) *Boundary Element Methods in Solid Mechanics*, George Allen and Unwin, London

Cruikshank,K.M., Zhao, G., and Johnson, A.M. (1991) Analysis of minor fractures associated with joints and faulted joints. *Journal of Structural Geology*, **13**, 865-866

Delaney, P.T., Miklius, A., Arnadotir, T., Okamura, A.T. and Sako, M.K. (1993) Motion of Kilauea Volcano during sustained eruption from Pu'u O'o and Kupaianaha vents, 1983-1991. *Journal of Geophysical Research*, **98**, 17801-17820

Duffield, W.A. (1975) Structure and origin of the Koae Fault System, Kilauea Volcano Hawaii. *United States Geological Survey Professional Paper 856*

Grant, J.V. and Kattenhorn, S.A. (2004) Evolution of vertical faults at an extensional plate boundary, southwest Iceland. *Journal of Structural Geology*, **27**, 537-557

Griffith, A.A. (1921) The phenomena of rupture and flow in solids. *Phil. Transactions of the Royal Society*, **A221**, 163-198

Gudmunsson, A. (1987) Tectonics of the Thingvellir fissure swarm, SW Iceland. *Journal of Structural Geology*, **9**, 61-69

Gudmundsson, A. and Bäckström, A. (1991) Structure and development of the Sveinagja graben, Northeast Iceland. *Tectonophysics*, **200** 111-125

Gudmundsson, A. (2000) Fracture dimension, displacements and fluid transport. *Journal of Structural Geology*, **22**, 1221-1231

Irwin, G.R. (1957) Analysis of Stresses and Strain Near the End of a Crack Traversing a Plate. *Journal of Applied Mechanics*, **24**, 361-364

Kassir, M.K. and Sih, G.C. (1966) Three-Dimensional Stress Distribution around an Elliptical Crack under Arbitrary Loadings. *Journal of Applied Mechanics*, **33**, 601-611

Kattenhorn,S.A., Aydin, A, and Pollard, D.D. (2000) Joints at high angles to normal fault strike: an explanation using 3-D numerical models of fault-preturbed stress fields. *Journal of Structural Geology*, **22**, 1-23

Kattenhorn, S.A. and Pollard, D.D. (1999) Is lithostatic loading important for the slip behaviour and evolution of normal faults in the Eart's crust? *Journal of Geophysical Research*, **104**, 28879-28898

King, G.C.P. and Nábêlek, J.L. (1985) The role of bends in faults in the initiation and termination of earthquake rupture, *Science*, **228**, 984-987

Lai, W.M., Rubin, D., and Krempl, E. (1993) *Introduction to Continuum Mechanics*, Butterworth, Woburn

Langley, J.S. (2001) Processes of normal faulting and surface deformation along the Koae Fault System, Hawai'i, M.S. Thesis, University of Hawai'i, Honolulu, Hawai'i

Lawn, B.R. and Wilshaw, T.R. (1975) *Fracture of Brittle Solids*, Cambridge University Press, New York

Lin, J. and Parmentier, E.M. (1988) Quasistatic propagation of a normal fault: A fracture mechanics model. *Journal of Structural Geology*, **10**, 249-263

Lipman, P.W., Lockwood, J.P., Okamura, R.T., Swanson, D.A. and Yamashita, K.M. (1985) Ground deformation Associated with the 1975 Magnitude 7.2 Earthquake and Resulting Changes in Activity of Kilauea Volcano, Hawai'i. *United States Geological Survey Professional Paper 1276*

Long, J.C.S and Witherspoon, P.A. (1985) The relationship of the degree of interconnection to permeability in fracture networks. *Journal of Geophysical Research*, **90**, 3087-3098

MacDonald, G.A. (1957) Faults and Monoclines on Kilauea Volcano, Hawaii. *Bulletin of the Geological Society of America*, **68**, 269-271

Martel, S.J. (1990) Formation of compound strike-slip fault zones, Mount Abbot quadrangle, California. *Journal of Structural Geology*, **12**, 869-882

Martel, S.J. (1997) Effects of cohesive zones on small faults and implications for secondary fracturing and fault trace geometry. *Journal of Structural Geology*, **19**, 835-847

Martel, S.J. (2004) Submarine landslides as a shear fracture phenomenon. *Marine Geology*, **203**, 319-339

Martel, S.J. and Boger, W.A. (1998) Geometry and mechanics of secondary fracturing around small three-dimensional faults in granitic rocks. *Journal of Geophysical Research*, **103**, 21299-21314

Martel, S.J. and Muller, J.R. (2000) A Two-dimensional Boundary Element Method for Calculating Elastic Gravitational Stresses in Slopes. *Pure and Applied Geophysics*, **157**, 989-1007

National Academy of Sciences (1996) Rock Fractures and Fluid Flow: Contemporary Understanding and Application. *National Research Council*, 551 pp, Washington, D.C.

Nicol, A., Watterson, J., Walsh, J.J. and Childs, C. (1996) The shapes, major axis orientations and displacement patterns of fault surfaces. *Journal of Structural Geology*, **18**, 235-248

Opheim, J.A. and Gudmunsson, A. (1989) Formation and geometry of fractures, and related volcanism, of the Krafla fissure swarm, northeast Iceland. *Bulletin of the Geological Society of America*, **101**, 1608-1622

Owen, S., Segall, P., Freymueller, J., Miklius, A., Denlinger, R., Árnadóttir, T., Sako, M. and Bürgmann, R.(1995) Rapid Deformation of the South Flank of Kilauea Volcano, Hawaii. *Science*, **267**, 1328-1332

Petit, J.P., Auzias, V., Rawnsley, K, and Rives, T. (2000) Development of joint sets in the vincinty of faults, in *Aspects of Tectonic Faulting*, edited by F.K. Lehner and J.L. Urai, Springer Verlag, 193-309

Pollard, D.D. and Aydin, A. (1984) Porpagation and linkage of Oceanic Ridge Segments. *Journal of Geophysical Research*, **89**, 10017-10028

Pollard, D.D. and Aydin, A. (1987) Progress in understanding jointing over the past century. *Geological Society of America Bulletin*, **100**, 1181-1204

Pollard, D.D., Segall, P., and Delaney, P. (1982) Formation and interpretation of dilatant echelon fractures in rock. *Geological Society of America Bulletin*, **93**, 1291-1303

Pollard, D.D, Delaney, P.T., Duffield, W.A., Endo, E.T. and Okamura, A.T. (1983) Surface deformation in volcanic rift zones. *Tectonophysics*, **94**, 541-584

Pollard, D.D. and Segall, P (1987) Theoretical displacements and stresses near fractures in rock: with applications to faults, joints, veins, dikes and solution surfaces, in *Fracture Mechanics of Rocks*, edited by B.K. Atkinson, Academic, San Diego

Rice, J.R. (1968) Mathematical Analysis in the mechanics of fracture, in *Fracture: An Advanced Treatise*, edited by H. Liebowitz, 191-311, Academic, San Diego

Rippon, J.H. (1985) Contoured patterns of throw and hade of normal faults in coal measures (Westphalian) of northeast Derbyshire. *Proceedings of Yorkshire Geological Society*, **45**, 147-161

Rubin, A.M. and Pollard, D.D. (1987) Origins of Blade-like Dikes in Volcanis Rift Zones. *United States Geologic Survey Professional Paper 1350*

Rudnicki, J.W. (1980) Fracture Mechanics applied to the Earth's crust. *Annual Review of Earth and Planetary Sciences*, **8**, 489-525

Rudnicki, J.W. and Wu, M. (1995) Mechanics of dip-slip faulting in an elastic half-space. *Journal of Geophysical Research*, **100**, 22173-22186

Segall, P. and Pollard, D.D. (1983) Mechanics of discontinuous faults. *Journal of Geophysical Research*, **85**, 4437-4350

Swanson, D.A., Duffield, W.A. and Fiske, R.S. (1976) Displacement of the south flank of Kilauea Volcano: the result of forcefull intrusion of magma into rift zones. textitUnited States Geological Survey Professional Paper 963

Tada, H, Paris, P.C. and Irwin, G.R. (2000) The Stress Analysis of Cracks Handbook, American Society of Mechanical Engineers, New York

Thomas, A.L. (1993) Poly3D: A three-dimensional, polygonal element, displacement discontinuity boundary element computer program with applicaitons for fractures, faults, and cavities in the Earth's crust, M.S. Thesis, Stanford University, Stanford, California

Walsh, J.J. and Watterson, J. (1988) Analysis of the relationship between displacements and dimensions of faults. *Journal of Structural Geology*, **10**, 239-247

Willemse, E.J.M. and Pollard, D.D. (2000) Normal fault growth: evolution of tipline shapes and slip distributions, in *Aspects of Tectonic Faulting*, edited by F.K. Lehner and J.L. Urai, Springer Verlag, 193-309

Wolfe, E.W. and Morris, J (1996) Geologic map of the island of Hawaii. *United States Geological Survey Map I-2524-A*